KaRIn: Ka-band Radar Interferometer

On-Board Processor (OBP)

Algorithm Theoretical Basis Document (ATBD)

JPL Document: D-79130

Revision B

August 3, 2021

Paper copies of this document may not be current and should not be relied on for official purposes. The current version is in the Product Data Management System (PDMS): https://pdms.jpl.nasa.gov/

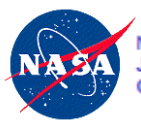

National Aeronautics and Space Administration
Jet Propulsion Laboratory
California Institute of Technology

KaRIn: Ka-band Radar Interferometer

On-Board Processor (OBP)

Algorithm Theoretical Basis Document (ATBD)

PREPARED BY (CUSTODIAN):

ELECTRONIC SIGNATURE ON FILE *9/30/2021*

_____ _____

Eva Peral / KaRIn Instrument System Engineer Date

APPROVED BY:

ELECTRONIC SIGNATURE ON FILE *9/30/2021*

_____ _____

Daniel Esteban-Fernandez / KaRIn Instrument Manager Date

EMAIL APPROVAL IN EPDM *10/04/2021*

_____ _____

Lee-Lueng Fu /SWOT Project Scientist Date

ELECTRONIC SIGNATURE ON FILE *10/10/2021*

_____ _____

Nacer Chahat / Payload System Engineer Date

Change Number	Change Date	Changes / Notes
JPL_KaRIn_OBP_ATBD_v1.docx	Aug. 6, 2014	Initial Draft
JPL_KaRIn_OBP_ATBD_v2.docx	Nov. 18, 2014	Updated sections 5.2 and 7.2
JPL_KaRIn_OBP_ATBD_v2a.docx	Nov. 21, 2014	Draft Release
D-79130_KaRIn_OBP_ATBD_Prelim_20160328	Mar. 28, 2016	Updated NEPA disclaimer. Preliminary Release.
D-79130_KaRIn_OBP_ATBD_Prelim_20160623	June 27, 2016	Updated baseline products resolution/posting. Updated Doppler centroid estimation. Pages 12,33,34 & 45
D-79130_KaRIn_OBP_ATBD_Initial_20160627	June 27, 2016	Initial released draft
D-79130_KaRIn_OBP_ATBD_RevA_20171103	Nov 11, 2017	RevA. Removed computation of the range compression reference function on board. Added robustness products. Added illustration to explain the systematic phase bias. Added option of canned Doppler centroid correction.
D-79130_KaRIn_OBP_ATBD_RevB	Feb 2, 2021	RevB. Removed errors in cross references. Beyond eq 11, time used for coregistration is kept explicit in the formulas.
	Mar 10, 2021	Added more detail to OBP product definition.
	July 6,2021	Added channel info to extra products
	Aug 3, 2021	Corrected typos. Added info on which analysis is done with 1km posting/resolution (section 4). Updated description of calibration paths (section 6.1).

EPDM ELECTRONIC SIGNATURE

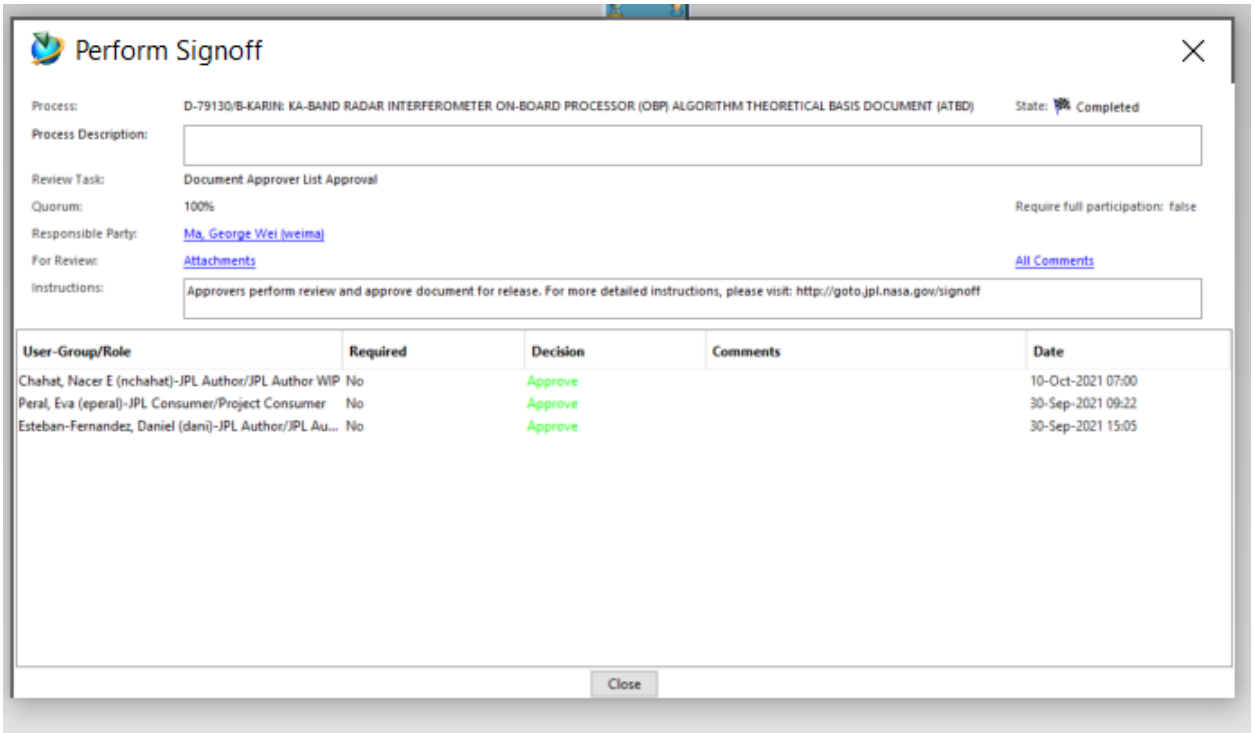

Table of Contents

List of Acronyms

AASR	Azimuth Ambiguity to Signal Ratio
BW	Chirp bandwidth
CTU	Control and Timing Unit
DORIS	Doppler Orbitography and Radio positioning Integrated by Satellite
ECCO2	Estimating the Circulation and Climate of the Ocean, Phase II
HW	Hardware
ISLR	Integrated Sidelobe Ratio
KaRIn	Ka-band SAR interferometric radar
MLE	Maximum Likelihood Estimator
MSS	Mean Sea Surface
N_B	Number of beams produced during azimuth compression
N_P	Number of pulses used for azimuth compression
OBC	On-Board Computer
OBP	On-Board Processor
PBW	Processing Bandwidth
RMS	Root Mean Square
SADC	Science Analog to Digital Converter
SAR	Synthetic Aperture Radar
S/C	Spacecraft
SLA	Sea Level Anomaly
SWOT	Surface Water and Ocean Topography
WGS84	World Geodetic System 1984

1 Introduction

The Surface Water and Ocean Topography (SWOT) mission has been recommended by the National Research Council decadal review "Earth Science and Applications from Space: National Imperatives for the Next Decade and Beyond" for implementation by NASA. The SWOT mission is a partnership between two communities, physical oceanography and hydrology, to share high vertical accuracy topography data produced by the payload configuration, whose principal instrument is the Ka-band Radar Interferometer (KaRIN). The broad scientific goals specified by the NRC decadal review have been refined by community involvement in open workshops and the guidance of an informal science team and can be summarized as follows.

Oceanography: characterize the ocean mesoscale and submesoscale circulation determined from the ocean surface topography at spatial resolutions of 15 km (for 68% of the ocean).

Hydrology: To provide a global inventory of all terrestrial surface water bodies whose surface area exceeds $(250m)^2$ (goal: $(100m)^2$, threshold: $1km^2$) (lakes, reservoirs, wetlands) and rivers whose width exceeds 100m (goal: 50m, threshold: 170m). To measure the global storage change in terrestrial surface water bodies at sub-monthly, seasonal, and annual time scales. To estimate the global change in river discharge at sub-monthly, seasonal, and annual time scales.

This document describes the SWOT On-board processing (OBP). The OBP processes the incoming radar signal from an interferometric channel pair and generates a complex interferogram using a set of parameters provided by the OBC (On-board computer), to be downlinked to the ground, and amplitude images for each channel. The on-board processor performs multi-look averaging to decrease the data rate over the oceans before downlink by about three orders of magnitude.

2 On-Board Processor Key Requirements

The OBP requirements are traced back to the following requirements on the **SWOT Science Requirements Document** (JPL D-61923).

2.4.1 [Requirement] The Baseline Science Mission shall operate for at least 42 months, including three annual cycles (36 months), a 3-month phase of launch/early operation and payload check out, and a 3-month fast-sampling calibration phase (including orbit transition).

2.5.3.a [Requirement] The SWOT orbit shall be a repeat orbit with a maximum repeat period of 23 days and a minimum repeat period of 21 days.

2.5.3.b [Requirement] The SWOT orbit ground track shall be controlled to within +/- 1 km at least 90% of each year, and not exceed +/- 2.5 km.

2.6.2.a [Requirement] The following Level-2 standard data products shall be produced for the ocean data in a grid covering the entire measurement swath and the nadir gap:

1.Ocean sea surface heights (SSH)

2.Estimated sea surface height uncertainties (1σ) on the same grid as the SSH measurements.

3.Radar σ0 measurements on the same grid as the SSH measurements.

4. Wind speed (but not direction) estimates derived from the radar σ0 on the same grid as the SSH measurements.

5. Nadir altimeter data products consistent with the Jason-series Geophysical Data Records (GDR's).

2.7.1.a [Requirement] The spatial posting of sea surface height measurements shall be no coarser than 2 km.

2.7.1.b [Goal] The spatial posting of height measurements will be no coarser than 250 m.

2.7.2.a [Requirement] The sea surface height error spectrum (cross-track average of the along-track spectra computed at different cross-track locations over the swath) in the wavelength range smaller than 1,000 km shall not exceed the spectrum envelope given in Figure 1 and the formulas below. This requirement holds for significant waveheights (SWH) less than 2 meters.

$$E(f) = 2 + 0.00125f^{-2}[cm^2/cycle/km] \quad 15km < \lambda < 1{,}000km$$

2.7.2.b [Goal] The white noise component of the error spectrum will not exceed 1cm^2/cycle/km.

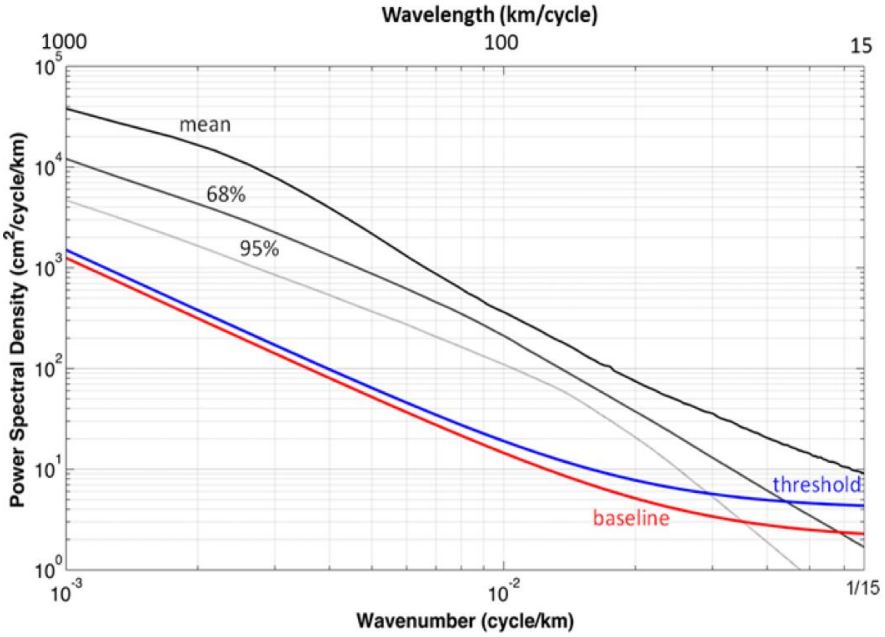

Figure 1: SSH baseline requirement spectrum (red curve) as a function of wavenumber. Blue curve is the threshold requirement. Shown, for reference is the global mean SSH spectrum estimated from the Jason-1 and Jason-2 observations (thick black line), the lower boundary of 68% of the spectral values (the upper gray dotted line), and the lower boundary of 95% of the spectral values (the lower gray dotted line). The intersections of the two dotted lines with the baseline spectrum at ~ 15 km (68%) and ~ 25 km (95%) determine the resolving capabilities of the SWOT measurement. The respective resolution for the threshold requirement is ~ 20 km (68%) and ~ 30 km (95%).

The mission architecture includes a Ka-band SAR interferometric (KaRIn) radar measuring two swaths, 50 km each, on each side of the nadir track, in non ping-pong operation mode (Figure 2). Each swath is covered with a different polarization, transmitted alternatively. The interferogram is computed between simultaneous pulses from the same swath but received by opposite antennas. The **baseline SWOT system parameters** are specified in Table 1. The requirements flow from the Science Requirements Document as sub-allocated through the project requirements down to the KaRIn instrument and the OBP, which have been used to derive OBP Functional and Performance Requirements.

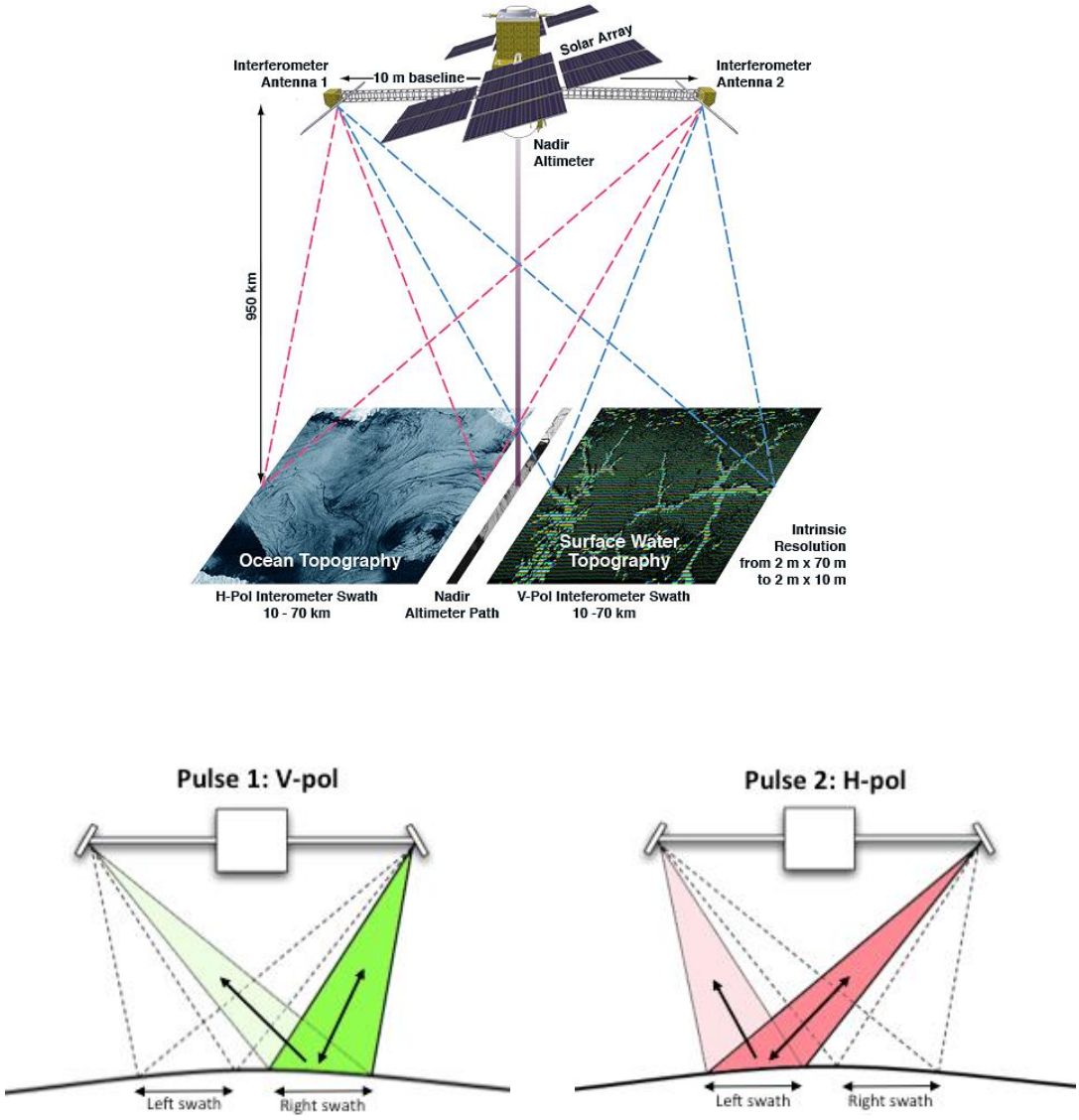

Figure 2: SWOT architecture and KaRIn non ping-pong operation mode.

SYSTEM PARAMETER	VALUE
Nominal platform height (at 45deg latitude)	906 km
Inclination	78 deg
Spacecraft orbital velocity	7372 m/s
Transmit center frequency	35.75 GHz
Transmit linear chirp bandwidth	200 MHz
Sampling frequency	300 MHz
PRF (per swath)	4420 Hz
Antenna boresight in elevation	2.65 deg
Antenna azimuth beamwidth (3 dB one-way)	0.1 deg
Baseline length	10.0 m
Ground range swath	10 to 60 km
Peak transmit power (EOL)	1500 W
Pulse length	6.4 μsec

Table 1: SWOT KaRIN System parameters

2.1 OBP Functional Requirements

- *Input*.
  - The OBP shall interface and receive two I/Q echoes (one from each channel) in real-time from the Science Analog to Digital Converters (SADCs).
  - The OBP shall interface with the SADCs to receive I/Q calibration pulses for three different calibration paths (see Section 6.1).

- *Processing*
  - The OBP shall range compress each pulse in real-time using a stored reference range function.
  - The OBP shall perform time co-registration between the channels.

- The OBP shall perform a range-independent filtering of the overlapping channel spectra between input channels during range compression, and range-dependent phase flattening.
- The OBP shall perform Doppler Centroid estimation (fractional part only).
- The OBP shall perform unfocused squinted SAR azimuth compression in real time. The Doppler centroid used for Doppler removal shall be the Doppler Centroid estimated on board plus a Doppler centroid correction computed from the Doppler centroid prediction stored in a canned table. The Doppler centroid prediction table can be re-uploaded from the ground.
- The OBP shall perform complex interferogram formation.
- The OBP shall perform along- and cross-track averaging.
- The OBP shall compute the average of each of the three calibration paths (see Section 6.1) at each averaging boundary (AV) of 3240 range lines.

- *Product generation*

The OBP will produce the following products:

- A complex interferogram product of the two input channels and power SAR images for each of the two input channels for each swath and nine azimuth beams.
  - Approximately 500mx500m ground resolution (full-width half-maximum correlation) and 250m posting.
  - Overlapping apodized averaging in both cross track and along track (section 6.8).
  - The pixels are centered at cross track distances from 5km to 64.75km for a total of 240 pixels.
  - Azimuth posting is 162 range lines.
  - The cross-track averaging ranges are computed on the fly based on the platform altitude from DORIS and the topography height from the topography table.
- The doppler used during ocean processing.
  - Along track averaging interval specified in on-board static parameter table, always a multiple of an averaging boundary (or 3240 range lines).

- Two coefficients corresponding to a linear fit over cross track.
- The sign of the doppler phase is such that with increasing range, the phase decreases (ignoring wrapping).

- The average of each of the three calibration paths.
  - Tx_LB for each channel (plus/minus) and each swath (H/V)
  - Cal_Rx for each channel (plus/minus) and each swath (H/V)
  - HB_cal for each channel (plus/minus) as the average of both swaths (H/V).

Per SDT/ADT recommendation, the OBP will also compute the following additional products for one channel (plus or minus) selectable through the static parameter table:

- Average SAR image power and SAR image power variance (average of SAR image power squared) for the center beam for each swath.
  - Approximately 250m x 250m ground resolution and 250m posting.
  - Non-overlapping rectangular averaging.
  - The pixels are centered at cross track distances 4.75km to 64.5km for a total of 240 pixels.
  - Azimuth posting is 162 range lines.
  - The cross-track averaging ranges are computed on the fly based on the platform altitude from DORIS and the topography height from the topography table.
  - Enables ground algorithms to detect/flag anomalous pixels (rain/ships/coastal and ice boundaries, etc.) and stress cases over the oceans at higher resolution than the interferograms, where detection may not be possible.
- Doppler centroid complex image for each swath from range compressed data computed as the average in cross track and along track of the complex multiplication of one range line and the complex conjugate of the next range line.
  - Approximately 2km x 2km pixels and 2km posting.
  - Non-overlapping rectangular averaging.

- The pixels cross track averaging is hard coded (not computed on the fly). It corresponds approximately to pixels centered from 10km to 56km for a total of 24 pixels.
    - First averaging index for ocean window starting at the ocean data window position (DWP) (1-based index): 104 154 215 285 366 457 558 669 790 921 1062 1213 1374 1546 1727 1919 2120 2332 2554 2785 3027 3279 3541 3813
    - Averaging window size: 50 61 70 81 91 101 111 121 131 141 151 161 172 181 192 201 212 222 231 242 252 262 272 281
- Azimuth posting is 1296 range lines.
- The sign of the doppler phase is such that with increasing range, the phase increases (ignoring wrapping), so opposite to the doppler used for ocean processing.
- Enables ground algorithms to extract ocean velocities with the potential to improve science return beyond current performance requirements.

- *Output*. The OBP shall interface with and deliver the output products to the Solid State Recorder Interface (SSRI) board.

2.2 OBP Performance Requirements

The OBP introduces random errors due to imperfect time co-registration, geometric and angular decorrelation (see section 5 and 6), as well as possible differences between the floating point model of the algorithm and the hardware implementation. The OBP also introduces errors originating from the dynamic part of the algorithm (section 7), such as the update rate of the coefficients describing the mean sea surface. The OBP errors are folded into the overall KaRIn performance requirements.

2.3 OBP Operating Requirements

- The OBP shall accept commands and triggers from the CTU (Control and Timing Unit) to process the incoming data.
- The OBP shall accept processing parameters from the OBC (On-board Computer) to process the incoming data.

3 Algorithm Description Overview

This section provides a high-level overview of the OBP algorithm (a description in pseudo-code can be found in Appendix E). In order to better understand the algorithm, it is recommended that the reader becomes acquainted with some of the background literature on SAR interferometry [1]-[5].

The OBP algorithm block diagram is illustrated in Figure 3. The two received echoes (one from each channel) in I/Q format from the SADC board are processed independently. The processing steps are as follows:

1. Range compression (i.e. matched filtering via an FFT match filter).
    a. Compute the FFT of the zero padded radar echo.
    b. Perform complex multiplication of the radar echo's FFT with the reference function.
    c. Compute the inverse FFT on the resulting signal.
    d. Discard throwaway region.
2. Range dependent sinc interpolation for the transmit channel to achieve time co-registration between the channels.
3. Doppler centroid estimation (fractional part) using the phase-based estimation method [6] on the raw data. This estimate is used during azimuth compression to re-center the Doppler spectrum approximately at 0 Hz to minimize SNR loss.
    a. Multiply each other range line with the complex conjugate of the previous range line.
    b. Complex average in azimuth and range to specified resolutions.
    c. Compute the phase and unwrap it.
    d. Compute a linear fit to the phase as a function of cross track distance.
4. N_P (number of lines to use in azimuth compression) range-compressed lines are corner-turned and stored in memory since the next steps operate in the azimuth direction, processing one range gate at a time for a number of consecutive pulses.
5. Squinted unfocused azimuth SAR processing for each collection of range gates from a series of consecutive pulses.
    a. Perform complex multiplication of the N_P azimuth samples by N_B phase ramps that take into account the Doppler centroid to shift the Doppler spectrum to N_B different Doppler angles
    b. Perform azimuth averaging to obtain N_B slices of the Doppler spectrum.

6. Compute the interferogram for each one of the N_B output beams by multiplying the compressed signal of one channel by the conjugate of the other channel.
7. Range dependent interferogram phase flattening. The phase ramp corresponds to the interferometric phase of a spherical reference surface that is slowly adjusted along the orbit to account for platform altitude and topographic variations.
8. Compute the image power for each one of the N_B output beams and for each channel by multiplying the compressed signal by its conjugate.
9. Perform multi-look averaging of the interferogram and the images power to achieve the required 500m (along-track) x 500m (cross-track) resolution at 250m posting.
10. Send the data to the Solid State Recorder interface board.

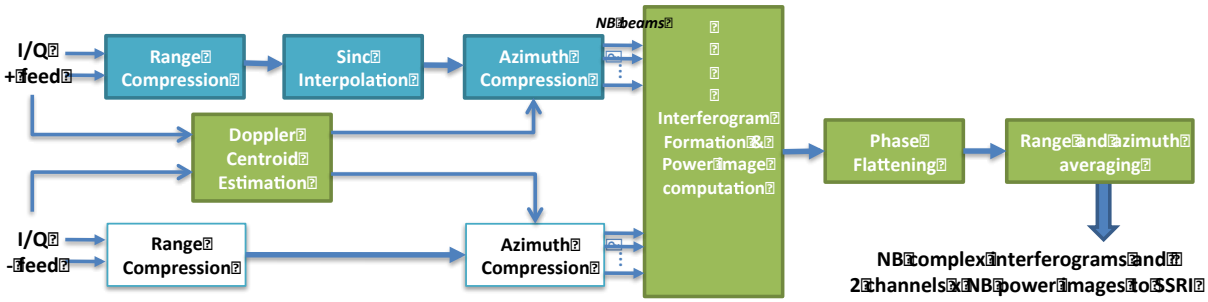

Figure 3. On-Board Processor block diagram for the case that the + feed is transmitting

As part of the ground processing, the following corrections are required to compensate for some of the OBP simplifications and other error sources that introduce biases. Information on the spacecraft attitude is needed to perform these corrections.

1. Remove the angular systematic bias that results from the iso-range lines and the iso-phase lines not being aligned.
2. Resampling of the beams to adjust for the different viewing geometries.
3. Compute height for each beam correcting for the slightly different baselines.
4. Perform optimal beam averaging.

4 Clarification on performance analyses in this ATBD

All performance analyses in this ATBD were produced with the previous baseline resolution and posting of 1km. The sections that have been updated to reflect the new 500m resolution/250m posting are the following:

- Section 2
- Table 4

Note that, for continuity, KaRIn System Engineering (SE) has continued to report random performance at 1km pixels in project reviews, even after changing the baseline resolution to 500m. That's also consistent with all the height error figures in this ATBD. The height error at 500m resolution is approximately twice the error at 1km resolution.

Also note that the performance analyses included in this ATBD were produced with an early simulated antenna pattern (not the measured FM patterns), with an initial estimate for the SNR error budget and with the initial requirements for pointing. All performance numbers are only included for illustration purposes, but they are not indicative of final performance.

The analyses in this ATBD assume pitch control 0.066deg 1-sigma and 0.2deg 3-sigma. The current requirement is 0.033deg 1-sigma and 0.1deg 3-sigma.

The following sections clarify some of the major deviations relative to the final implementation of KaRIn.

4.1 Section 5.3

Since we are not using the FM measured patterns, the dispersion and sidelobe levels will be similar but not identical to those illustrated in the figures.

4.2 Section 5.4

The analyses in this section are impacted by the fact that they were performed with 1km resolution/posting and with an early simulated antenna pattern. The systematic phase bias shape and systematic height errors will be similar but not identical to those illustrated in the figures. This could be most evident on the height bias error in Figure 17 and Figure 18 because of the smaller 500m resolution and especially for the 100m slick.

4.3 Section 6

Figure 22-Figure 24 were computed with early antenna patterns and SNR error budget. The conclusion still remains that the 3240 range lines provide sufficient performance to compute the doppler centroid estimation over the ocean.

The same applies to Figure 31. In addition, this height error is computed for a 1km pixel rather than a 500m pixel.

Figure 32 and Figure 33 correspond to 1km pixel resolution. The blue, red and green curves can be easily scaled in the x-axis direction to approximately obtain the response for 500m pixel resolution. For Figure 32, the autocorrelation will be 0.5 around 250m rather than 500m. For Figure 33, the -3dB point will happen at around 1cy/km rather than 0.5cy/km.

The analysis shown in Figure 34-Figure 41 is high level and intended to illustrate the impact of the point target response in the height error. This analysis is not intended to verify any OBP requirement and a re-analysis of these results at 500 resolution is therefore unnecessary. The finer 250m posting will make it easier to remove contaminated pixels, and additional filtering can be performed to achieve similar results to those shown for 1 km pixels.

4.4 Section 7 - Section 9

All the height error plots in these sections (Figure 4, Figure 47, Figure 51, Figure 55) correspond to 1km pixels and initial SNR error budget and antenna patterns, so they do not represent final performance.

5 Algorithm Mathematical Formulation

This section presents a derivation of the expected value for the interferogram. It is based on the work by Prati, Gatelli, et. al. [7],[8], which is known as the wavenumber shift algorithm.

We choose a coordinate system centered at the middle of the interferometric baseline and at the center of the azimuth aperture, i.e. $m = 0$, where m is an index used to identify each pulse forming the azimuth aperture, $m = -\frac{N_P-1}{2} \ldots \frac{N_P-1}{2}$ and N_P, assumed to be an odd number, is the number of pulses used for azimuth compression. The return signal for pulse m for the right, $v_1^{(m)}$, and left, $v_2^{(m)}$, channels after demodulation can be modeled as follows:

$$v_i^{(m)}(t) = \iint_{S(\vec{r})} A(r)\Gamma_i(\vec{r})s(\vec{r})p_i\left(t - \frac{2\bar{r}_i^{(m)}}{c}\right)e^{-j2k\bar{r}_i^{(m)}}dS + n_i^{(m)}(t) \quad (1)$$

where:

- p_i is the transmit pulse received by the i-th channel.
- $\bar{r}_i^{(m)}$ is the one-way range distance to a point target on the surface $S(\vec{r})$ for the echo received by the i-th channel and the m pulse.
- $k = {}^{2\pi}/_{\lambda}$ is the propagation factor, λ is the wavelength and c is the speed of light.
- $n_i^{(m)}$ is the thermal noise for the i-th channel, assumed to be an uncorrelated white noise process.
- $A(r)$ is an amplitude factor that depends weakly on range.
- $s(\vec{r})$ represents the surface brightness. It depends weakly on the platform position through its dependence on incidence angle.
- Γ_i is the two-way antenna far field complex gain, including far field phase

For SWOT geometry, and since N_P is a small number (baseline is 9), the platform position dependence of $A(r)$, $\Gamma_i(\vec{r})$, and the range point target response (see χ_{r_i} below) can be ignored.

After range compression, and ignoring for now the noise contribution, we get:

$$v_i^{(m)}(t) = \iint_{S(\vec{r})} A(r)\Gamma_i(\vec{r})s(\vec{r})\chi_{r_i}\left(t - \frac{2\bar{r}_i^{(m)}}{c}\right)e^{-j2k\bar{r}_i^{(m)}}dS \quad (2)$$

where $\chi_{r_i}(t)$ is the i-th channel range point target response. The Fourier transform of the range point target response, $W_i(\omega)$, is given by:

$$\chi_{r_i}(t) = \frac{1}{2\pi}\int W_i(\omega)e^{j\omega t}d\omega \quad (3)$$

$$W_i(\omega) = P_i(\omega)P_{ref_i}^*(\omega) \quad (4)$$

where $P_i(\omega)$ is the Fourier transform of the transmit pulse received by the i-th channel and $P_{ref_i}(\omega)$ is the corresponding range compression reference function in the Fourier domain.

As stated in [7], the backscattered signal for the two different viewing geometries contains different spectral components of the ground reflectivity (this is further explained later in this section). The noise contribution from the disjoint part of the spectra can be avoided by filtering the common band of the two signals prior to computing the interferogram. The optimum filtering is range dependent. However, given SWOT's parameters, the improvement from performing range dependent filtering is not significant and does not justify the increased hardware complexity. Instead, the reference function for each channel is optimized to remove the non-common portion of the two spectra and minimize the coherence loss for

the complete swath. The reference function is also used to remove the phase of the electronic components in the calibration path.

Since the receiving antennas are separated by a baseline, each antenna receives the echo for a given scatterer at different times. In order to avoid the decorrelation introduced by this time delay, after range compression the interferometric signals are co-registered in time. Equation (2) can be rewritten as:

$$v_i^{(m)}(t) = \iint_{S(\vec{r})} A(r)\Gamma_i(\vec{r})s(\vec{r})\chi_{r_i}\left(t - \frac{2\bar{r}_i^{(m)}}{c} - \Delta_i\right)e^{-j2k\bar{r}_i^{(m)}}dS \tag{5}$$

The antenna patterns are assumed to be much broader in the range direction than the system range spacing so that, for any given range cell, they can be considered as essentially constant. The radar echoes can be locally expanded for each range cell centered at time $t_0 = \frac{2}{c}r_0$ such that $t = t_0 + \tau$ where $\tau = \frac{2}{c}\delta r$. Any point on the reference sphere can be defined by its ground range, ρ, and its azimuth angle, φ. The deviation in ground range, $\delta\rho$, of the surface point at ρ_0 corresponding to range distance r_0 is given by:

$$\delta\rho = \frac{\delta r}{\sin\theta_{i0}} \tag{6}$$

where θ_{i0} is the incidence angle at r_0. Similarly, $\bar{r}_i^{(m)} = \bar{r}_{i0}^{(m)} + \delta\rho\,\overline{\sin\theta_{ii}}$, where $\overline{\sin\theta_{ii}}$ is the mean of the sines for the transmit and return path incidence angles for the viewing geometry of channel i. The integral equation (5) becomes:

$$v_i^{(m)}(\tau) = \frac{c}{2\sin\theta_{i0}}\iint A(r_0)\Gamma_i(\rho_0,\varphi)s\left(\rho_0 + \frac{c}{2\sin\theta_{i0}}\tau',\varphi\right)$$
$$\chi_{r_i}\left(\tau - \frac{2\bar{r}_{i0}^{(m)} - 2r_0}{c} - \Delta_i - \frac{\overline{\sin\theta_{ii}}}{\sin\theta_{i0}}\tau'\right)e^{-j2k\left(\bar{r}_{i0}^{(m)} + \frac{\overline{\sin\theta_{ii}}}{\sin\theta_{i0}}\frac{c}{2}\tau'\right)}\rho_0 d\varphi d\tau' \tag{7}$$

Let $S(\omega,\varphi)$ be the Fourier transform of the terrain reflectivity $s\left(\rho_0 + \frac{c}{2\sin\theta_{i0}}\tau',\varphi\right)$. By computing the Fourier transform of (7), we obtain the following [9]:

$$V_i^{(m)}(\omega) = \frac{c}{2\sin\theta_{i0}} \int A(r_0)\Gamma_i(\rho_0,\varphi) S\left((\omega+\omega_0)\frac{\overline{\sin\theta_{ii}}}{\sin\theta_{i0}}, \varphi\right) W_i(\omega) \\ e^{-j2k\bar{r}_{i0}^{(m)}} e^{-j\omega\left(\frac{2\bar{r}_{i0}^{(m)}-2r_0}{c}+\Delta_i\right)} \rho_0 d\varphi \tag{8}$$

The reflectivity spectrum, $S(\omega,\varphi)$, can be assumed to have a white Gaussian distribution. This is consistent with the deep phase approximation in rough surface scattering, $\langle s(\vec{r})s(\vec{r}')\rangle = \delta(\vec{r}-\vec{r}')\sigma_0(\vec{r})$ where $\sigma_0(\vec{r})$ is the normalized radar cross-section per unit surface, which applies when the surface RMS roughness is large compared to the wavelength. Notice that we assume that the radar cross section varies over scales much greater than the range resolution so that, for a given range cell, only azimuth variations need to be considered.

Equation (8) demonstrates that the received terrain reflectivity spectrum is stretched and shifted for one viewing geometry relative to the other. For SWOT geometry, the stretching is small and can be neglected. The shift is given by:

$$w_i = \omega_0 \frac{\overline{\sin\theta_{ii}} - \sin\theta_{i0}}{\sin\theta_{i0}} \tag{9}$$

In order to calculate the interferometric correlation, one must evaluate the expectation value of the channel cross-product. From (8) we obtain:

$$\langle v_1^{(m)}(\tau) v_2^{(n)*}(\tau)\rangle \cong \left(\frac{c}{2\sin\theta_{i0}}\rho_0\right)^2 \iint d\varphi\, d\varphi' |A(r_0)|^2 \Gamma_1(\rho_0,\varphi)\Gamma_2^*(\rho_0,\varphi') e^{-j2k\left(\bar{r}_{10}^{(m)}-\bar{r}_{20}^{(n)}\right)} \\ \left(\frac{1}{2\pi}\right)^2 \iint d\omega\, d\omega' e^{-j\omega\left(\frac{2\bar{r}_{10}^{(m)}-2r_0}{c}+\Delta_1\right)+j\omega'\left(\frac{2\bar{r}_{20}^{(n)}-2r_0}{c}+\Delta_2\right)+j(\omega-\omega')\tau} \\ \langle S(\omega+\omega_0+w_1,\varphi) S^*(\omega'+\omega_0+w_2,\varphi')\rangle W_1(\omega) W_2^*(\omega') \tag{10}$$

Using the deep phase approximation in rough surface scattering, equation (10) simplifies as:

$$\langle v_1^{(m)} v_2^{(n)*} \rangle \Big|_{t_0}$$
$$= \frac{c}{2\sin\theta_{i0}} \frac{1}{2\pi} \iint d\varphi \, d\omega \, \rho_0 |A(r_0)|^2 \Gamma_1(\rho_0,\varphi) \Gamma_2^*(\rho_0,\varphi) \sigma_0(\rho_0,\varphi) e^{-j2k\left(\bar{r}_{10}^{(m)} - \bar{r}_{20}^{(n)}\right)} \tag{11}$$
$$W_1(\omega - w_1) W_2^*(\omega - w_2) e^{-j(\omega - w_1)\left(\frac{2\bar{r}_{10}^{(m)} - 2r_0}{c} + \Delta_1\right) + j(\omega - w_2)\left(\frac{2\bar{r}_{20}^{(n)} - 2r_0}{c} + \Delta_2\right)}$$

SWOT operates in non ping-pong mode. Without loss of generality, we consider the case that the right antenna is transmitting with the boresight pointing to the right swath. In that case, the following expressions hold:

$$\Gamma_1(\vec{r}) = G_1(\vec{r})$$

$$\Gamma_2(\vec{r}) = (G_1(\vec{r}) G_2(\vec{r}))^{1/2}$$

where $G_i(\vec{r})$ represents the i-th antenna one-way far field complex gain (including far field phase),

$$\Delta_1 = \frac{B}{c} \sin\theta_0 \equiv \Delta$$

$$\Delta_2 = 0$$

with θ_0 the look angle for a target at r_0 on the reference spherical surface and B the interferometric baseline,

$$\bar{r}_{10}^{(m)} = r_{10}^{(m)}$$

$$\bar{r}_{20}^{(m)} = \frac{r_{10}^{(m)} + r_{20}^{(m)}}{2}$$

with $r_i^{(m)}$ the range from the i-th antenna to a point target on the surface $S(\vec{r})$ for the m pulse,

$$\overline{\sin\theta_{i1}} = \sin\theta_{i1}$$

$$\overline{\sin\theta_{i2}} = \frac{\sin\theta_{i1} + \sin\theta_{i2}}{2} \cong \sin\theta_{i0}$$

where θ_{ii} is the incidence angle for the viewing geometry of the i-th antenna,

$$w_1 \cong -\omega_0 \frac{B\cos\theta_0 \cos\varphi}{2r\tan\theta_{i0}} = -w$$

$$w_2 \cong 0$$

With these approximations, (11) becomes:

$$\langle v_1^{(m)} v_2^{(n)*} \rangle\Big|_{t_0}$$
$$= \frac{c}{2\sin\theta_{i0}} \frac{1}{2\pi} \iint d\varphi\, d\omega\, \rho_0 |A(r_0)|^2 \Gamma_1(\rho_0,\varphi)\Gamma_2^*(\rho_0,\varphi)\sigma_0(\rho_0,\varphi) e^{-jk\left(2r_{10}^{(m)} - r_{10}^{(n)} - r_{20}^{(n)}\right)} \tag{12}$$
$$W_1(\omega + w) W_2^*(\omega) e^{-j\frac{\omega}{c}\left(2r_{10}^{(m)} - r_{10}^{(n)} - r_{20}^{(n)}\right) - j\frac{W}{c}\left(2r_{10}^{(m)} - 2r_0\right) - j(\omega+w)\Delta}$$

Let $r^{(m)}$ be the distance from the middle of the platform to a target at a distance r for platform position m. Then, for the SWOT geometry, we can well approximate:

$$r_0 \cong \frac{r_{10} + r_{20}}{2}$$
$$r_{10}^{(m)} \cong r^{(m)} - \frac{\delta r^{(m)}}{2} \tag{13}$$
$$r_{20}^{(m)} \cong r^{(m)} + \frac{\delta r^{(m)}}{2}$$
$$\delta r^{(m)} = r_{20}^{(m)} - r_{10}^{(m)} \cong B\, \vec{l}^{(m)} \cdot \vec{\beta} \cong B\, \vec{l} \cdot \vec{\beta} \equiv \delta r$$

Note that δr contains the topography information that SWOT is going to measure, whereas $(r_{20} - r_{10})$ is the range difference for the reference sphere that is used for time co-registration and phase flattening.

Using the approximations (13) in (12) we obtain:

$$\langle v_1^{(m)} v_2^{(n)*} \rangle\Big|_{t_0}$$
$$= \frac{c}{2\sin\theta_{i0}} \frac{1}{2\pi} \iint d\varphi\, d\omega\, \rho_0 |A(r_0)|^2 \Gamma_1(\rho_0,\varphi)\Gamma_2^*(\rho_0,\varphi)\sigma_0(\rho_0,\varphi) e^{-j2\left(k + \frac{\omega}{c}\right)\left(r^{(m)} - r^{(n)}\right) + jk\delta r} \tag{14}$$
$$e^{-j2\frac{W}{c}\left(r^{(m)} - r_0\right)} W_1(\omega + w) W_2^*(\omega) e^{-j(\omega+w)\left(\Delta - \frac{\delta r}{c}\right)}$$

In SWOT's OBP, the phase flattening is applied before multi-look averaging. However, for the purposes of simplifying the analytical formulas, we include it now in the formulation. The range dependent flattening phase is given by $e^{-j\Omega}$, where Ω is as follows:

$$\Omega = kB\sin\theta_0 = \omega_0 \Delta$$

This is equivalent to

$$\Delta = \frac{\delta r_0}{c}$$

$$\Omega = \omega_0 \frac{\delta r_0}{c}$$

where δr_0 is our best estimate of the difference in range from the second and first antenna to the spherical reference surface.

After phase flattening (14) is simplified as:

$$\langle v_1^{(m)} v_2^{(n)*} \rangle\Big|_{t_0} = \frac{c}{2\sin\theta_{i0}} \frac{1}{2\pi} \iint d\varphi\, d\omega\, \rho_0 |A(r_0)|^2 \Gamma_1(\rho_0,\varphi)\Gamma_2^*(\rho_0,\varphi)\sigma_0(\rho_0,\varphi) \tag{15}$$
$$W_1(\omega+w)W_2^*(\omega) e^{-j2\left(k+\frac{\omega}{c}\right)\left(r^{(m)}-r^{(n)}\right)-j2\frac{w}{c}\left(r^{(m)}-r_0\right)} e^{-j\left(k+\frac{\omega+w}{c}\right)(\delta r_0-\delta r)}$$

There remains a small time decorrelation caused by the topography and by interfering pulses from different platform positions, both of which are small for SWOT. There is also a phase error due to this time misregistration that is proportional to the frequency centroid of the interferometric signal, ω_c,

$$\omega_c = \frac{\int \omega\, |W_1(\omega+w)W_2^*(\omega)| d\omega}{\int |\, W_1(\omega+w)W_2^*(\omega)| d\omega}$$

In the ideal case of perfectly square pulses, $\omega_c \cong -\frac{w}{2}$

Equation (15) becomes:

$$\langle v_1^{(m)} v_2^{(n)*} \rangle\Big|_{t_0} = \frac{c}{2\sin\theta_{i0}} \frac{1}{2\pi} \iint d\varphi\, d\omega\, \rho_0 |A(r_0)|^2 \Gamma_1(\rho_0,\varphi)\Gamma_2^*(\rho_0,\varphi)\sigma_0(\rho_0,\varphi) \tag{16}$$
$$W_1(\omega+w)W_2^*(\omega) e^{-j2\left(k+\frac{\omega_c}{c}\right)\left(r^{(m)}-r^{(n)}\right)-j2\frac{w}{c}\left(r^{(m)}-r_0\right)} e^{-j\left(k+\frac{\omega_c+w}{c}\right)(\delta r_0-\delta r)}$$

Squinted, Doppler-sharpened (unfocused) azimuth SAR processing is then performed: N_B beams are formed by applying different phase ramps in time to a collection of N_P pulses, each one followed by a low-pass filter. The phase ramps also include a phase term to remove a range dependent Doppler centroid, f_D, which is hereafter assumed to be estimated correctly. The phase ramps correspond to equally spaced delays of the form $e^{-j2\pi m\left(\frac{J}{N_P}+\frac{f_D}{PRF}\right)}$, $m = -\frac{N_P-1}{2} \ldots \frac{N_P-1}{2}$. This is effectively equivalent to performing an FFT in azimuth direction and shifting the spectrum to 0 Hz (i.e., removing the shift associated with the

Doppler centroid in the azimuth spectrum). The indexes J correspond to slicing the processed portion of the azimuth spectrum into N_B different sub-beams, each one with a different azimuth center, which correspond to N_B predetermined azimuth look directions. Given that for each sub-beam we are only interested in the signal in the center slice of the shifted spectrum, the subsequent low-pass filter can be simply implemented by performing a weighted average of the frequency shifted samples with an window, w_m, which for SWOT is rectangular as a baseline. As a result, after azimuth compression, N_B beams are generated.

Without loss of generality, and for simplicity in the notation, we assume $f_D = 0$. Let $u_i^{(J)}$ be the signal corresponding to the resulting *J*-th sub-beam for channel i, which can be represented mathematically as:

$$u_i^{(J)} = \sum_m e^{-j2\pi m\frac{J}{N_P}} w_m v_i^{(m)}$$

Note that *J* does not need to be an integer, since we might not slice the spectrum uniformly, or might only process part of the spectrum.

The interferometric correlation after azimuth compression for the *J*-th sub-beam is thus given by,

$$\begin{aligned}&\langle u_1^{(J)}(\tau) u_2^{(J)*}(\tau)\rangle\Big|_{t_0}\\ &\cong \frac{c}{2\sin\theta_{i0}}\int |A(r_0)|^2 \Gamma_1(\rho_0,\varphi)\Gamma_2^*(\rho_0,\varphi)\sigma_0(\rho_0,\varphi)\chi_{az}^{(J)}(\rho_0,\varphi)e^{-j\left(k+\frac{\omega_c+w}{c}\right)(\delta r_0-\delta r)}\rho_0 d\varphi\end{aligned} \tag{17}$$

$$\frac{1}{2\pi}\int W_1(\omega+w)W_2^*(\omega)d\omega$$

where the azimuth point target response for the *J*-th sub-beam, $\chi_{az}^{(J)}$, is defined as follows:

$$\chi_{az}^{(J)}(\vec{r}) = \sum_{m,n} e^{-j2\pi(m-n)\frac{J}{N_P}} w_m w_n\, e^{-j2\left(k+\frac{\omega_c}{c}\right)\left(r^{(m)}-r^{(n)}\right)-j2\frac{w}{c}\left(r^{(m)}-r_0\right)} \tag{18}$$

The complex correlation coefficient for beam (J) is defined as:

$$\gamma^{(J)} = \frac{\langle u_1^{(J)} u_2^{(J)*}\rangle}{\sqrt{\langle u_1^{(J)} u_1^{(J)*}\rangle \langle u_2^{(J)} u_2^{(J)*}\rangle}} \tag{19}$$

and can be expressed as the product of three terms, $\gamma_N^{(J)}$, $\gamma_\varphi^{(J)}$, γ_g, which are commonly referred to as the noise, angular, and geometric correlation, respectively:

$$\gamma^{(J)} = \gamma_N^{(J)}\gamma_\varphi^{(J)}\gamma_g \tag{20}$$

where

$$\gamma_N^{(J)} = \frac{1}{\sqrt{\left(1 + {}^{1}\!/_{SNR_1^{(J)}}\right)\left(1 + {}^{1}\!/_{SNR_2^{(J)}}\right)}} \tag{21}$$

$$\gamma_g = \frac{\int W_1(\omega + w) W_2^*(\omega) d\omega}{\sqrt{\int |W_1(\omega + w)|^2 d\omega \int |W_2(\omega)|^2 d\omega}} \tag{22}$$

$$\gamma_\varphi^{(J)} = \frac{\int \Gamma_1(\rho_0, \varphi) \Gamma_2^*(\rho_0, \varphi) \sigma_0(\rho_0, \varphi) \chi_{az}^{(J)}(\rho_0, \varphi) e^{-j\left(k + \frac{\omega_c + w}{c}\right)(\delta r_0 - \delta r)} d\varphi}{\sqrt{\left(\int |\Gamma_1(\rho_0, \varphi)|^2 \sigma_0(\rho_0, \varphi) \chi_{az}^{(J)}(\rho_0, \varphi) d\varphi\right)\left(\int |\Gamma_2(\rho_0, \varphi)|^2 \sigma_0(\rho_0, \varphi) \chi_{az}^{(J)}(\rho_0, \varphi) d\varphi\right)}} \tag{23}$$

In equation (21), $SNR_i^{(J)}$ is the system signal-to-noise ratio for channel i and *J*-th sub-beam.

The Cramer-Rao bound for the phase variance can be shown to be [4]:

$$\langle \Delta\Phi^2 \rangle = \frac{1}{2N_{looks}} \frac{1 - \gamma^2}{\gamma^2} \tag{24}$$

This limit is approached asymptotically as the number of looks, N_{looks}, increases. Equation (24) is only true when the looks are taken over independent samples. After spectral filtering, samples are no longer independent. The effective number of independent looks can be computed as:

$$N_{looks} = \frac{1}{BW} \frac{[\int |H(f)|^2 df]^2}{\int |H(f)|^4 df} \tag{25}$$

where $H(f)$ is the transfer function for the radar response and BW is the range bandwidth. Equation (25) was derived for a SAR power image [16], but it can be shown that it is also a good approximation for the number of independent interferometric looks.

From this analysis, the error budget for the OBP can be split into two categories:

1. *Random error,* associated with decorrelation and loss of effective looks
2. *Systematic bias error*, associated with a bias that cannot be corrected on the ground

5.1 Angular correlation

The angular correlation term, $\gamma_\varphi^{(J)}$, in equation (23), introduces a systematic phase bias, which can be corrected if the antenna pattern is known, and a small amount of decorrelation. These are due to the fact that iso-range lines and iso-interferometric-phase lines are only approximately aligned, so the interferometric fringes vary over the range cell, even after the phase flattening (see Figure 4c).

In the following analysis, the impact of the wavenumber shift on the interferometric phase is ignored, although it can be easily incorporated by using an effective wavenumber. The phase factor in the angular correlation, $\Phi = -k(r_2 - r_1 - \delta r)$, is the interferometric phase, and contains the topography height information that SWOT measures.

It is important to understand the magnitude of the systematic phase bias, and its sensitivity to antenna pattern errors and sigma-0 variations. In the following derivations we use the spherical coordinate system illustrated in Figure 5. To simplify notation, we assume the interferometric baseline is aligned with the crosstrack (the generalization is straight forward). From (13) we obtain:

$$\delta r = B \sin\theta \cos\varphi$$

The interferometric phase can thus be decomposed into systematic phase bias, Φ_{syst}, and a topographic phase, Φ_{topo}, as follows:

$$\begin{aligned} \Phi &= \Phi_{syst} + \Phi_{topo} \\ \Phi_{syst} &= -kB \sin\theta_0 \,(1 - \cos\varphi) \\ \Phi_{topo} &= -kB(\sin\theta_0 - \sin\theta)\cos\varphi \end{aligned} \tag{26}$$

To first order, Φ_{topo} is proportional to topography height, h, as follows:

$$\Phi_{topo} \approx \kappa_z \cos\varphi \, h \tag{27}$$

where $\kappa_z = \frac{kB\cos\theta_0}{r\sin\theta_{i0}}$.

The systematic bias for a spherical surface is illustrated in Figure 50. It does not converge to zero in the far range because the spherical surface does not have the same radius as the reference surface.

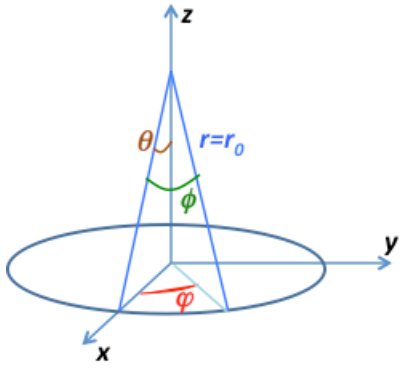

(a)

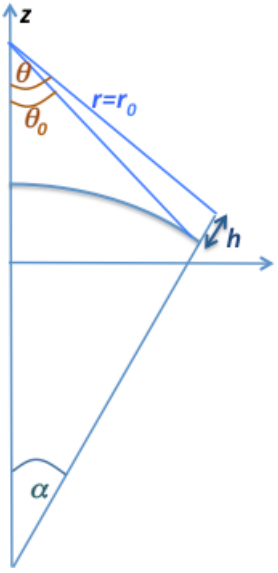

(b)

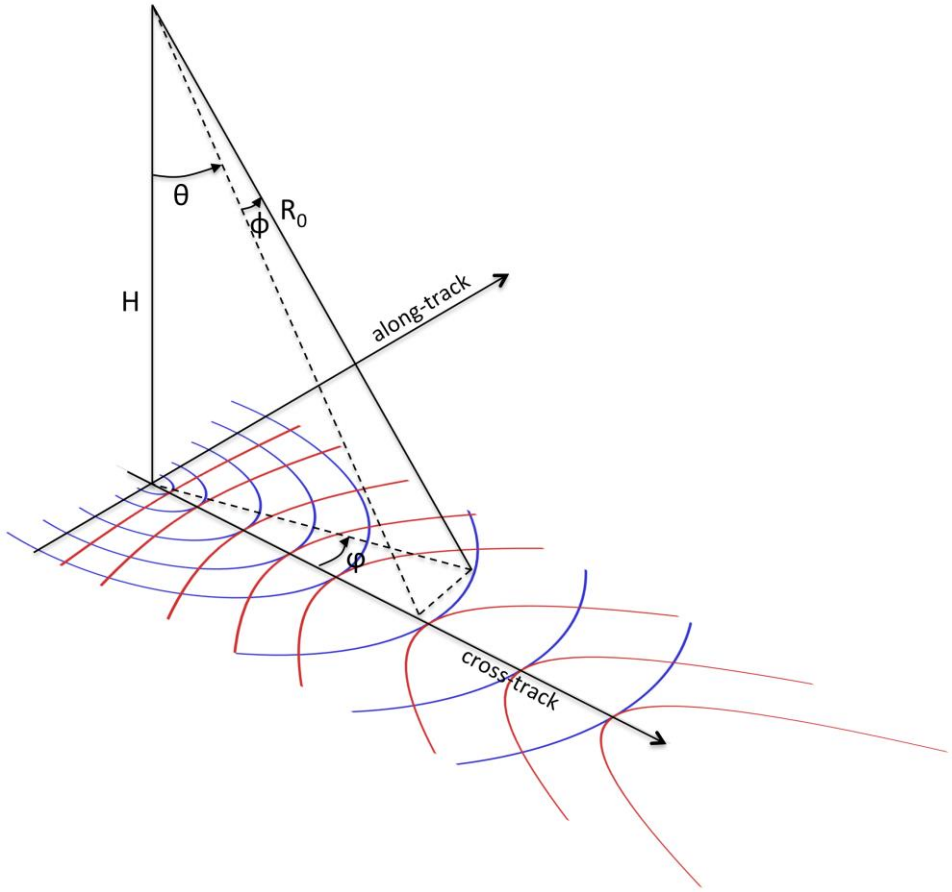

(c)

Figure 5. Coordinate system used in the mathematical formulation. On (a) the axis **x** is aligned with cross-track and **y** with along-track. The circle represents the intersection of the spherical reference surface with the iso-range lines, all points of which are at a constant angle, θ. We define three angles: the look angle, θ, the ground azimuth angle, φ, and the antenna azimuth angle, ϕ. Figure (b) illustrates a cut along the plane containing the nadir vector and a target at a given height *h* over the reference sphere. (c) Pictorial representation of iso-rangelines (blue) vs. iso-interferometric-phase lines (red).

5.2 Sensitivity analysis for angular correlation

In order to gain further insight into the magnitude and sensitivities of the systematic phase bias and angular decorrelation, in this section we derive an analytical solution for $\gamma_{\varphi}^{(J)}$ by approximating the product of antenna gain, sigma-0 and azimuth point target response as a Gaussian function of φ centered at φ_J and with variance σ_J.

$$\Gamma_1(\vec{r})\Gamma_2^*(\vec{r})\sigma_0(\vec{r})\chi_{az}^{(J)}(\vec{r}) \approx A\frac{1}{\sqrt{2\pi}\sigma_J}e^{-\frac{1}{2}\left(\frac{\varphi-\varphi_J}{\sigma_J}\right)^2}$$

Expanding $\cos\varphi$ around φ_J we obtain:

$$1-\cos\varphi \approx 1-\cos\varphi_J+\sin\varphi_J\,(\varphi-\varphi_J)+\frac{1}{2}\cos\varphi_J\,(\varphi-\varphi_J)^2$$

This integral can be analytically solved and the end result is:

$$\gamma_{\varphi}^{(J)}=\frac{1}{\sqrt{1+jkB\sigma_J^2\sin\theta_0\cos\varphi_J}}e^{\frac{-\frac{1}{2}(kB\sigma_J\sin\theta_0\sin\varphi_J)^2}{1+jkB\sigma_J^2\sin\theta_0\cos\varphi_J}-jkB\sin\theta_0(1-\cos\varphi_J)}$$

The systematic phase bias is given by the phase of $\gamma_{\varphi}^{(J)}$, and the decorrelation by its absolute value. We can simplify:

$$\left|\gamma_{\varphi}^{(J)}\right| \approx e^{-\frac{1}{2}(kB\sigma_J\sin\theta_0\sin\varphi_J)^2}$$

$$\measuredangle\gamma_{\varphi}^{(J)} \approx -\frac{1}{2}kB\sigma_J^2\sin\theta_0\cos\varphi_J-kB\sin\theta_0\left(1-\cos\varphi_J\right)\approx-\frac{1}{2}kB\sin\theta_0\,(\sigma_J^2+\varphi_J^2) \tag{28}$$

It is convenient to express the systematic bias as a function of the antenna azimuth angle, ϕ, which is related to the ground azimuth angle, φ, as $\sin\phi=\sin\theta\sin\varphi$, or $\phi\cong\varphi\sin\theta$. If the product of antenna gain, sigma-0 and azimuth point response is expressed as a Gaussian function of ϕ centered at ϕ_J and with variance ϱ_J, then

$$\measuredangle\gamma_{\varphi}^{(J)} \approx -\frac{kB}{2\sin\theta_0}(\varrho_J^2+\phi_J^2)$$

and the associated systematic height, using (27), would be

$$h_{\varphi}^{(J)} \approx -\frac{H}{2}(\varrho_J^2+\phi_J^2)$$

which is approximately independent of cross track, since ϕ_J and ϱ_J do not exhibit a strong dependence on cross track. From this, one can derive the sensitivity of the systematic height to ϕ_J and ϱ_J as follows:

$$\frac{\partial h_{\varphi}^{(J)}}{\partial \phi_J} = -H\phi_J$$
$$\frac{\partial h_{\phi}^{(J)}}{\partial \varrho_J} = -H\varrho_J \quad (29)$$

The decorrelation is given by

$$\left|\gamma_{\phi}^{(J)}\right| \approx e^{-\frac{1}{2}\left(\frac{kB}{\sin\theta_0}\varrho_J\phi_J\right)^2}$$

and increases in the near range.

5.3 Antenna dispersion

In the previous analysis it was assumed that the antenna pattern was not dependent on the signal frequency. SWOT's antenna is dispersive, both in phase and amplitude, which impacts coherence, systematic phase bias, ambiguities, SNR and number of effective looks.

Figure 6-Figure 9 show the antenna dispersion in phase and magnitude, after subtracting the phase at boresight in elevation and 0 deg in azimuth. The dispersion in azimuth is higher than in elevation.

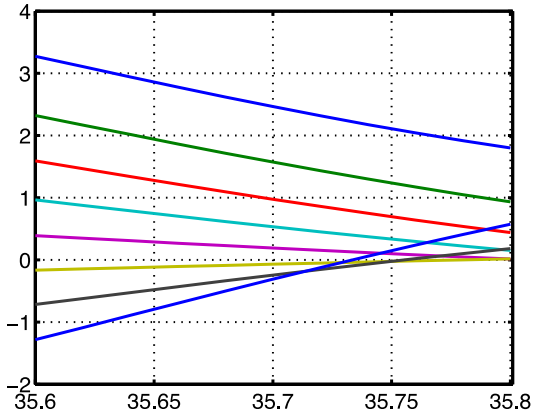

Figure 6. Antenna phase in elevation minus phase at boresight (2.65deg) as a function of frequency for various antenna elevation angles.

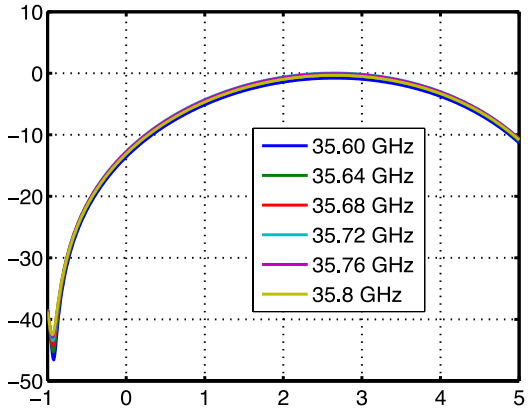

Figure 7. Antenna directivity in elevation as a function of elevation angle for various frequencies in the band.

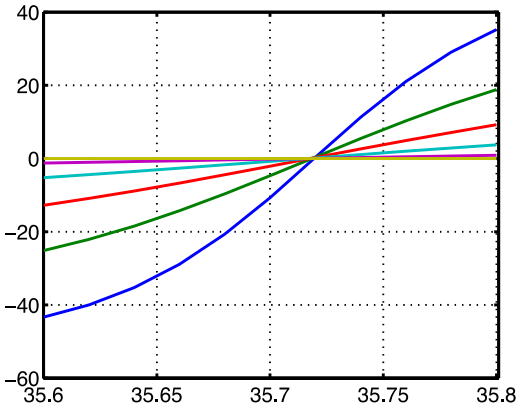

Figure 8. Antenna phase in azimuth minus phase at 0 deg as a function of frequency for several antenna azimuth angles.

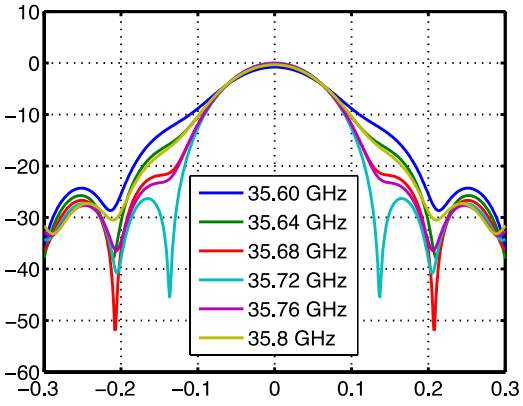

Figure 9. Antenna directivity in azimuth as a function of antenna azimuth angle.

In general, equation (17) becomes

$$\langle u_1^{(J)}(\tau)u_2^{(J)*}(\tau)\rangle\Big|_{t_0} \cong \frac{c}{2\sin\theta_{i0}}\oint_{r=r_0}|A(r)|^2\,\sigma_0(\vec{r})\chi_{az}^{(J)}(\vec{r})e^{-j\left(k+\frac{w}{c}\right)(\delta r_0-\delta r)} \tag{30}$$

$$\frac{1}{2\pi}\int \widetilde{W_1}(\vec{r},\omega+w)\widetilde{W_2^*}(\vec{r},\omega)e^{-j\frac{\omega}{c}(\delta r_0-\delta r)}d\omega\,ds$$

where

$$\widetilde{W_i}(\vec{r},\omega) = W_i(\omega)\Gamma_i(\vec{r},\omega)$$

The correlation, $\gamma^{(J)}$, is now given by:

$$\gamma^{(J)} = \gamma_N^{(J)}\cdot$$

$$\left(\oint_{r=r_0}\sigma_0(\vec{r})\chi_{az}^{(J)}(\vec{r})e^{-j\left(k+\frac{w}{c}\right)(\delta r_0-\delta r)}\int \widetilde{W_1}(\vec{r},\omega+w)\widetilde{W_2^*}(\vec{r},\omega)e^{-j\frac{\omega}{c}(\delta r_0-\delta r)}d\omega\,ds\right) \tag{31}$$

$$\cdot\frac{1}{\sqrt{\left(\oint_{r=r_0}\sigma_0(\vec{r})\chi_{az}^{(J)}(\vec{r})\int\left|\widetilde{W_1}(\vec{r},\omega+w)\right|^2 d\omega\,ds\right)}}$$

$$\cdot \frac{1}{\sqrt{\left(\oint_{r=r_0} \sigma_0(\vec{r})\chi_{az}^{(J)}(\vec{r}) \int \left|\widetilde{W_2}(\vec{r},\omega)\right|^2 d\omega\, ds\right)}}$$

The performance impact of the antenna dispersion in coherence, SNR and effective number of looks is negligible. The systematic phase bias, however, is strongly impacted by the antenna dispersion. This systematic bias will be estimated and corrected on the ground as a function of attitude and platform position and velocity. The details of this correction are included in the Algorithm Description Document of the Low Resolution product. The residual systematic phase bias error depends on our knowledge of the antenna pattern, sigma0 and attitude, and the sensitivity to these parameters will be discussed in section 5.4.

The spectral broadening due to dispersion increases the azimuth sidelobes, as illustrated in Figure 10. The impact on ambiguity will be explored in section 6.8.

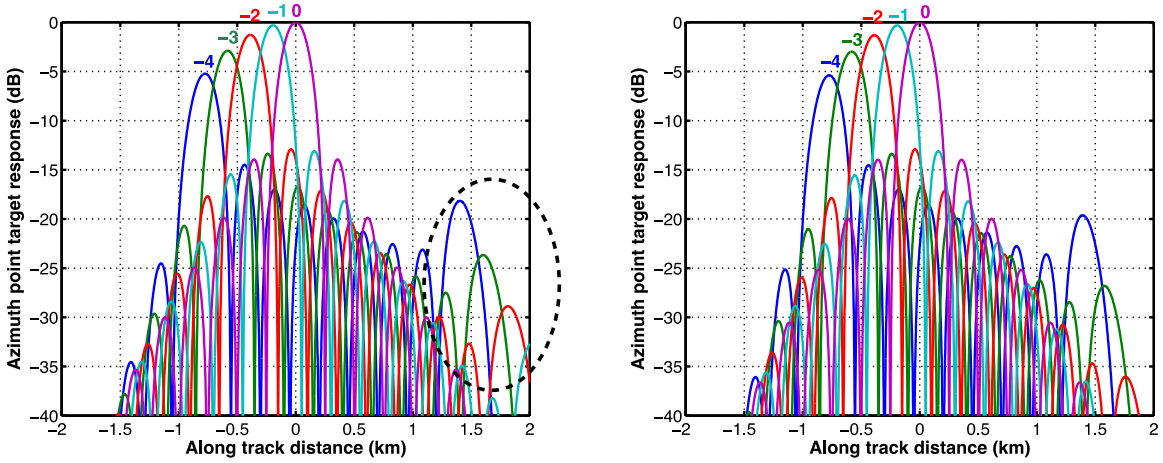

Figure 10. Antenna azimuth response with dispersion (left) and without (right). The dashed circle on the left plot indicates the region where sidelobes have significantly worsened due to the dispersion.

5.4 Systematic phase bias sensitivity analysis

Section 5.1 and 5.3 provided the theoretical basis to compute the systematic phase bias. As indicated in equation (29), this phase bias is sensitive to knowledge of the effective pointing angle and effective beamwidth, which is a result of combining the squinted beam azimuth response, the antenna response and sigma-0, as well as the antenna azimuth pointing angle. In this section, we investigate the sensitivity to these various factors through numerical simulations using the full antenna pattern including

dispersion effects. Note that this analysis is for information purposes only, since this error is not part of the OBP error budget, and is captured at a higher level.

Figure 11 depicts the typical systematic phase bias one would obtain for a spherical surface identical to the reference surface for beams 0 to 4 (beams -1 to -4 would be identical to 1 to 4 for the assumed symmetric antenna pattern). As illustrated in Figure 12, the systematic phase bias calculation needs to take into account the dispersive effects of the antenna pattern, and it is not sufficient to only consider the antenna pattern at the center frequency. The height error due to not considering the full antenna pattern would be ~1.5cm RMS over the swath.

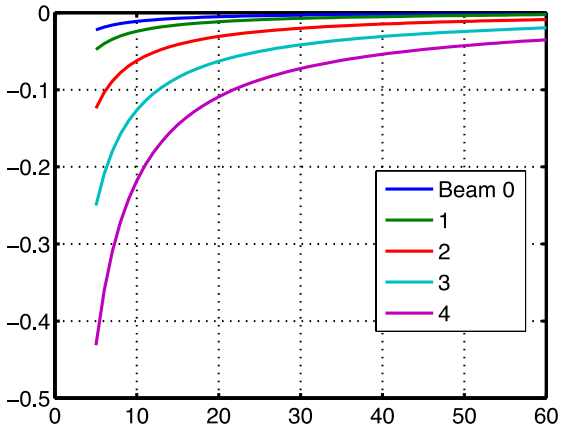

Figure 11. Systematic phase bias for spherical Earth.

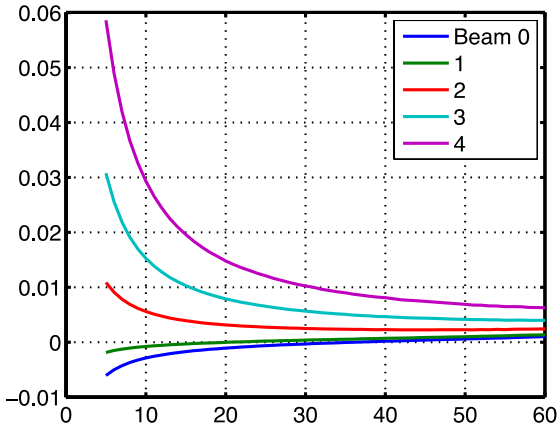

Figure 12. Difference between systematic bias for antenna with and without dispersion.

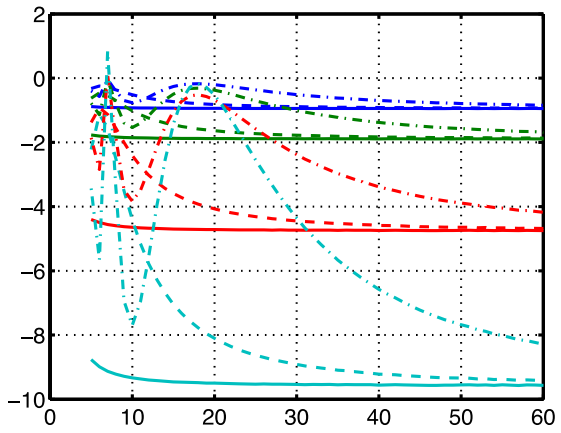

Figure 13. Systematic height bias as a function of cross track for various errors in the antenna azimuth beamwidth. Solid corresponds to no squint, dashed to 0.067deg (1-sigma) and dash-dotted to 0.2deg (3-sigma)

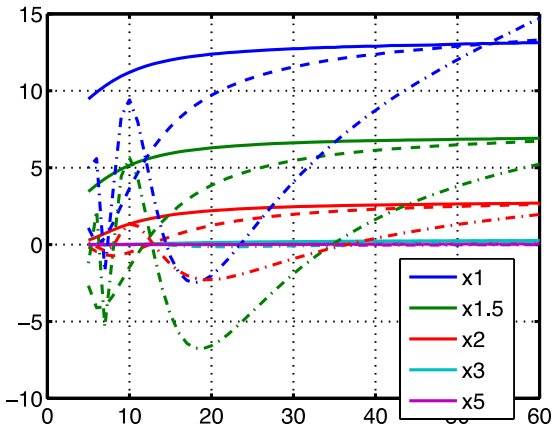

Figure 14. Impact of only knowing a portion of the antenna pattern in azimuth, given by the factor in the legend times the antenna 1-way 3dB beamwidth. Solid corresponds to no squint, dashed to 0.067deg (1-sigma) and dash-dotted to 0.2deg (3-sigma)

It is important to understand the sensitivity of the systematic phase bias to our knowledge of the antenna pattern. In order to evaluate this, we have studied the sensitivity of the systematic height bias to scaling the antenna pattern in azimuth. The beams are combined using the weights predicted from the MLE estimate (see Appendix B). As one can observe in Figure 13, for 1% antenna beamwidth error, the height error is less than 1mm, even for the 3-sigma squint angle of 0.2deg. A related but different question is how much of the antenna pattern has to be accurately characterized in order to be able to predict the systematic bias. As illustrated in Figure 14, at least 2 times the 3dB 1-way beamwidth (~0.1deg for SWOT) needs to be known to reduce the error to less than 2mm.

According to the analysis in section 5.2, the systematic height bias is approximately constant across the swath and, as predicted by equation (29), a squint in the antenna pointing has significant impact on the systematic phase bias. Figure 15 illustrates the systematic height bias for various squint angles, assumed to be constant across the swath, as would be the case of a pitch, as a function of cross track. The squint angle can drift along the orbit (requirement is 0.2deg 3-sigma), and estimates of the squint angle will be available on the ground from the S/C attitude control system (such as gyro and star tracker), from the on-board Doppler centroid estimate and from calibration, but there will still remain a small knowledge error. Figure 16 shows the height bias for various knowledge errors in the squint angle and for two different squint angles: 1-sigma squint angle (0.067deg in solid) and 3-sigma (0.2deg in dashed). Note that for large squint angles, and depending on the accuracy of the estimate, the ground processing algorithm might optimally decide to throw away the outer beams, which contribute the most to this error.

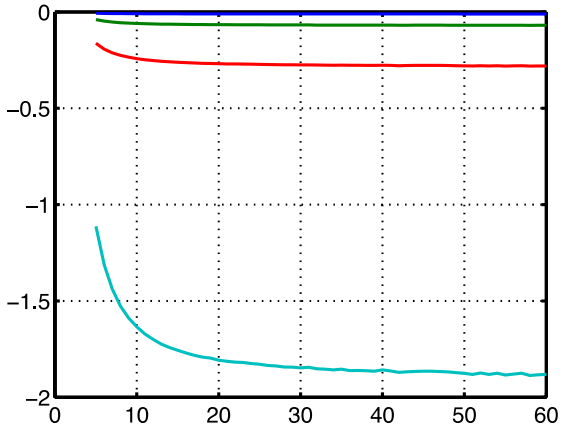

Figure 15. Systematic height bias as a function of cross track for various antenna squint angles (constant across swath).

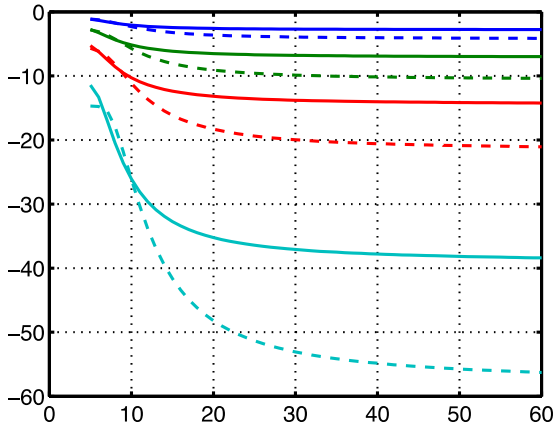

Figure 16. Systematic height bias as a function of cross track for various errors in the antenna squint angle (constant across swath) around the predicted squint angle, which is 0.067deg (1-sigma) for the solid curves and 0.2deg (3-sigma) for dashed curves.

As previously stated, variations in sigma-0 also distort the effective azimuth point target response and impact the systematic phase bias. Examples of those are ocean slicks and ocean streaks [10]. To better characterize the impact of these, we have computed the systematic phase bias analytically using equation (23) (and confirmed the results through higher fidelity simulations) for an ocean slick of a certain sigma-0 contrast relative to the surrounding area and aligned with the cross track. Since the systematic bias is larger for off-boresight angles, as the main beam, which contains most of the power, is steered away from boresight, the error increases significantly. The following plots illustrate the cases of no squint and the 1-sigma value (0.067deg). Figure 17 and Figure 18 illustrate the height bias as a function of distance of the S/C from the ocean slick for various slick widths and 4dB contrast. As shown in Figure 19 and Figure 20, the height bias is fairly insensitive to cross track distance. As expected, the stronger the contrast, the higher the height bias.

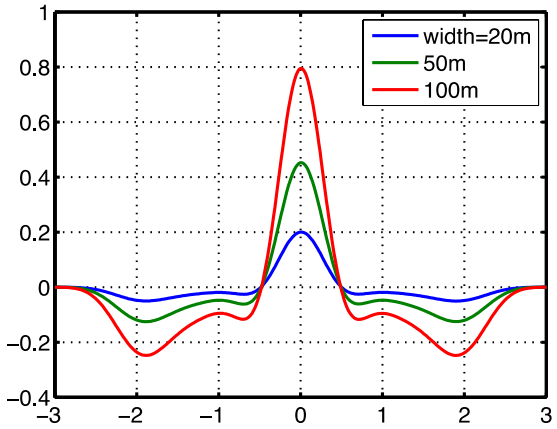

Figure 17. Height bias due to ocean slick of 4dB contrast as a function of distance of the S/C from the ocean slick for various slick widths and no squint.

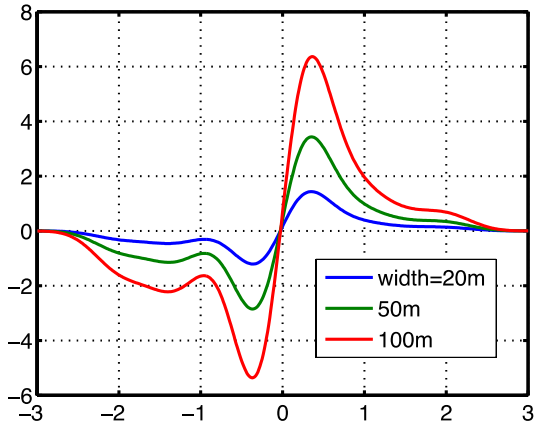

Figure 18. Height bias due to ocean slick of 4dB contrast as a function of distance of the S/C from the ocean slick for various slick widths and 0.067deg squint.

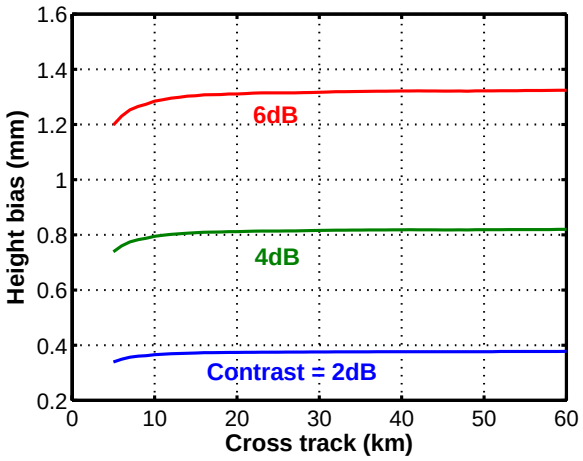

Figure 19. Height bias due to 100m wide ocean slick (worst case slick position) for several contrasts as a function of cross track distance for no squint.

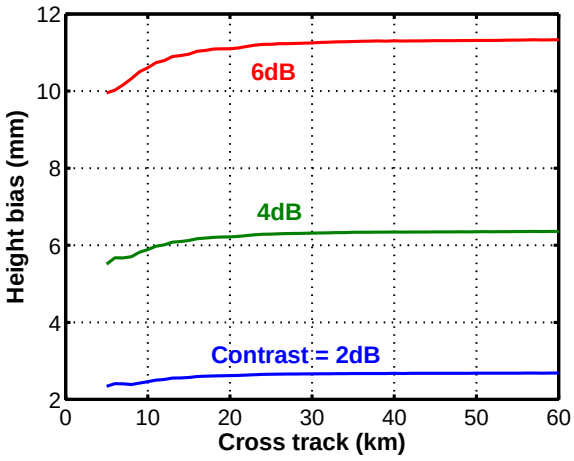

Figure 20. Height bias due to 100m wide ocean slick (worst case slick position) for several contrasts as a function of cross track distance for 0.067deg squint.

5.5 Ocean waves: the Volumetric Formulation

The statistics of the ocean surface can be modeled with a Gaussian probability function,

$$f_{sp}(h) = \frac{1}{\sqrt{2\pi\sigma_h^2}} e^{-\frac{h^2}{2\sigma_h^2}}$$

In this expression we have ignored skew and the electromagnetic bias, which could be introduced straightforwardly if needed. The parameter σ_h is the ocean standard deviation and is related to the significant wave height as $SWH = 4\sigma_h$. From (23), the volumetric correlation is approximately given by:

$$\gamma_v \cong \int e^{j\kappa_z h} f_s(h) dh = e^{-\frac{1}{2}\kappa_z^2 \sigma_h^2}$$

The formulation presented here gives a first order approximation of the effect of ocean waves. However, a more detailed analysis is presented in [18], which shows that, even though the decorrelation is well described by the volumetric formulation, the systematic bias is not, and needs to be accounted for as an additional error source.

6 Description of Static Algorithm

This section describes in detail each of the algorithm steps assuming fixed parameters for the geometry computations. Section 7 will explain how various parameters are adjusted along the orbit to account for platform and topographic variations.

6.1 Calibration path averaging

Figure 21 includes an illustration of KaRIn calibration paths.

At the top of Figure 21, we can see the timing diagram for the calibration paths for four Transmit Repetition Intervals (TRI), with TRI = 1/(2 PRF), each corresponding to sending either the H or the V polarization transmit pulse. For each of the TRIs, the OBP captures the transmit loopback path (TxLB) for the H and V polarizations. Then, alternating every 2 TRIs, it captures the receiver calibration path (calRx) and the Hyperbox calibration path (calHB). In all 3 cases, for both plus and minus channels are captured. The bottom plots show the path for each of these calibration signals.

- The transmit loopback calibration, TxLB, includes the hyberbox Tx (which generates the chirp and upconverts it to Ka band), the high power amplifier (HPA), part of the duplexer (which contains the front end switch assembly), the hyberbox Rx (which downconverts the chirp from Ka band to baseband) and KDES (which converts the analog signal to digital).
- The receiver calibration, calRx, includes the hyberbox Tx, the front-end low noise amplifier (LNA), the hyperbox Rx and KDES.
- The hyberbox calibration, calHB, includes the hyperbox Tx, hyperbox Rx and KDES.

There are components in the signal path that fall outside the calibration (represented by the Antenna block, although it includes other components as well), and components within the calibration loop that are not part of the signal path (represented by the calibration HW block). The three calibration signals do not follow identical paths through this calibration HW, so the impact is not the same and cannot be easily calibrated out, but it is expected to be small.

For the calHB path, there is no difference between the H and V signals (the signal path is identical in both time slots), so the signals in these two time slots are averaged together.

For each of these paths, an average signal is produced every averaging interval (AV), which corresponds to 3240 range lines (6480 TRIs). However, not all lines are used in the average, only 3230 range lines (6460 TRIs).

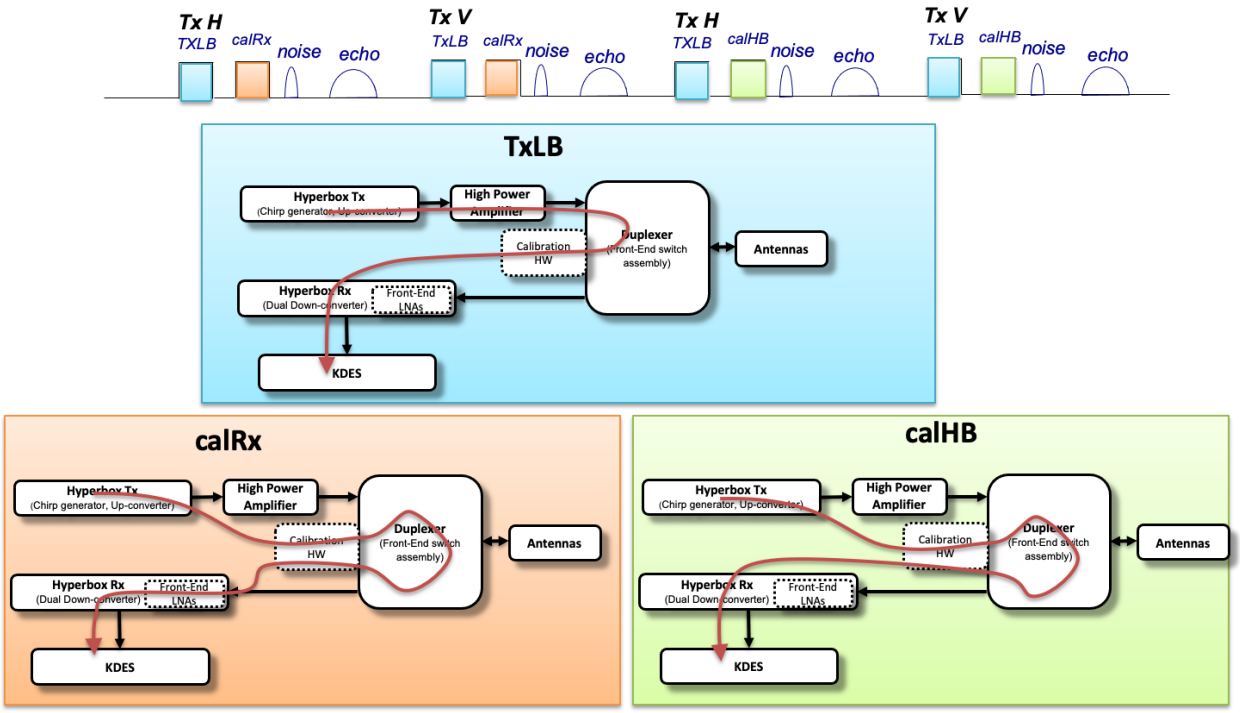

Figure 21. KaRIn calibration paths: transmit loopback (blue), receiver calibration (orange) and hyberbox calibration (green).

6.2 Doppler Centroid Estimation

The azimuth sampling rate, or PRF, limits the highest observable Doppler frequency; only frequencies between -0.5PRF and +0.5PRF can be observed. The Doppler frequency component in this range is referred to as the fractional Doppler Centroid. The fractional Doppler Centroid sets the azimuth compression filter center. Errors in the estimate of the fractional Doppler Centroid result in degradation of the SNR and the azimuth ambiguity to signal ratio (AASR). The Doppler ambiguity will not be estimated in the OBP, since it is only needed for calculating the systematic phase bias and geolocation, and can be computed on the ground based on the spacecraft attitude knowledge data or raw data captures.

The fractional Doppler Centroid is estimated in SWOT using a phase based method [6] applied on the raw data in order to make it more robust against bright targets. The difference of the signal phase from line to line is computed and averaged both in range an azimuth as described in Section 3. Figure 22 illustrates the correlation of the pulse pairs with and without thermal noise. A weighted linear fit to the calculated Doppler centroid is used for azimuth compression and sent to the ground together with the interferogram and power images. This will be used to extract the systematic phase bias and for geolocation during ground processing. Some important parameters that affect the performance of the Doppler centroid estimation are the length of the averaging windows in range and azimuth. Table 2 includes current OBP parameters for Doppler centroid estimation.

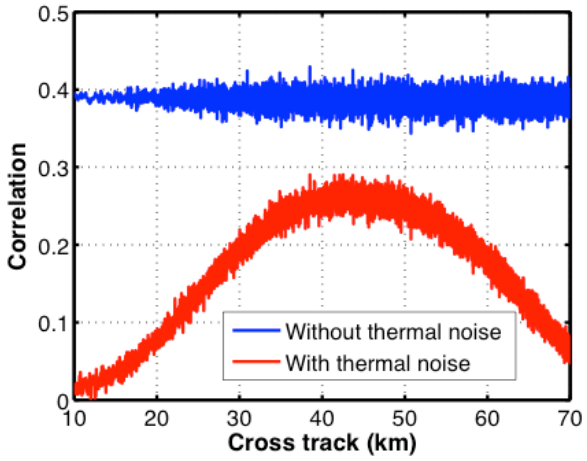

Figure 22. Pulse pair correlation as a function of cross track distance.

Due to HW resource considerations, rectangular averaging windows are used in both range and azimuth. In addition, a fixed reference ground range is used to fit and evaluate the doppler centroid (rather than computing the ground range on the fly, as for the interferogram range averaging). Since the ground range used to compute the fit and to evaluate the polynomial are the same, the error introduced by this approximation is negligible.

Two values are computed in cross track over two range intervals, and then averaged in along track. These two points are fit to a line as a function of the reference ground range by multiplication with a 2x2 matrix. The Doppler centroid estimate is computed by evaluating the fitted linear polynomial at the reference ground range. The indexes for the range intervals, the azimuth averaging length, the reference ground range and the fitting matrix are in an up-loadable static parameter table. Different azimuth averaging length and fitting matrix can be specified for land and ocean processing.

The accuracy requirement on the Doppler centroid estimation is given by the acceptable SNR loss (Figure 23) and increase in ambiguities (see section 6.8). To make impact of the Doppler centroid estimation error negligible, the Doppler centroid relative to the PRF will need to be estimated to better than 1%.

Figure 24 shows simulation results for the Doppler centroid estimation as a function of the number of processed azimuth lines, given the nominal SNR (1-sigma case). According to this, 100 lines would be enough to meet this requirement. Note that the Doppler due to wave and current motion has a small impact on performance.

Method	Phase based
Azimuth averaging window	Rectangular
Azimuth averaging window length (nominal)	3240 range lines for ocean
Range averaging window	Rectangular
Range averaging intervals (nominal)	30-45km and 45-60km

Table 2. Doppler centroid estimation algorithm parameters

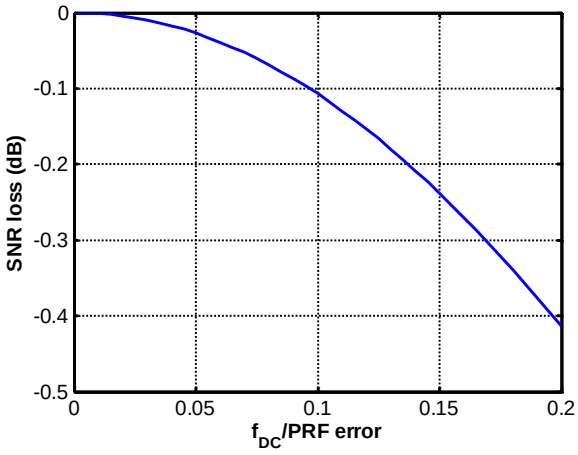

Figure 23. SNR loss due to error in Doppler centroid estimation.

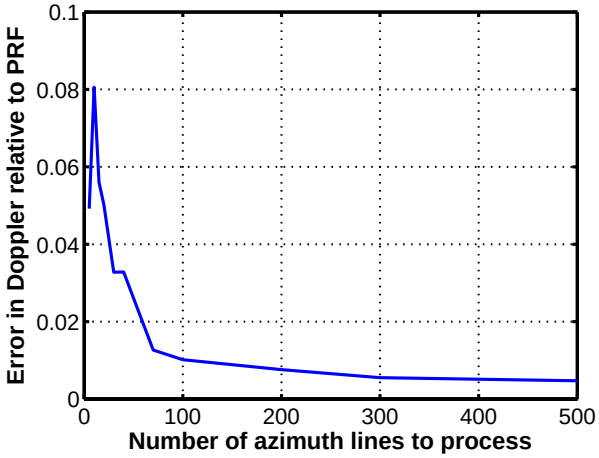

Figure 24. Doppler centroid estimation error (worst case in cross track) as a function of the number of processed azimuth lines.

6.3 Range Compression

The range compression, or matched filtering via an FFT match filter, is a central part of the algorithm. The slant range swath is ~3.1km at the equator. The maximum receive window (at the Equator) is ~25.4 μs, which corresponds to 7619 samples at 300 MHz sampling for a nominal pulse width of 4.5us. Therefore, the range compression implements an 8K FFT/IFFT.

The reference function used in range compression is different for each channel and it is a canned function stored in an uploadable table.

As explained in section 5, the range compression reference function also includes a filter that is optimized to remove the non-common portion of the two spectra and minimize the coherence loss for the complete swath, and is offset for each channel as shown in Figure 25. Currently, the filter bandwidth is 196MHz.

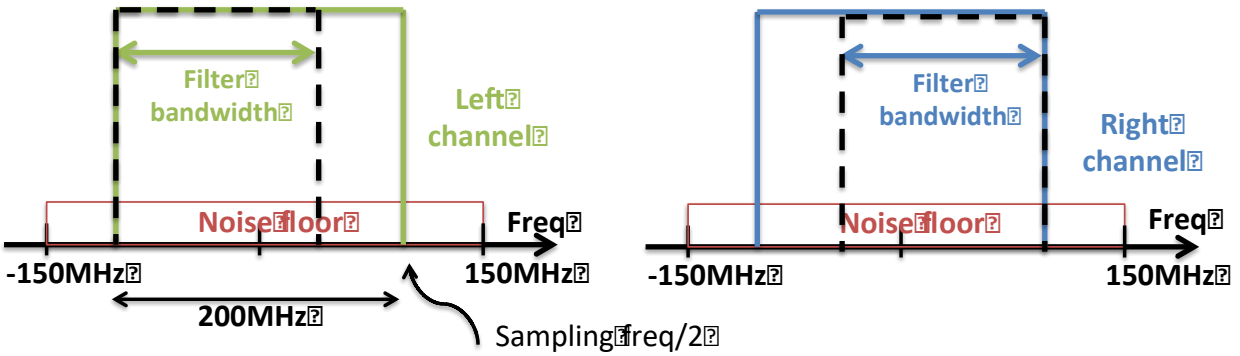

Figure 25. Filter bandwidth for left and right channels to optimize geometry correction.

An important consideration in the range compression step is the selection of a range window to improve the integrated side-lobe ratio, or ISLR, and the peak side-lobe ratio, or PSLR. Improved ISLR and PSLR come at the expense of a reduction in the number of looks that degrades the random error. It is worth noting that even though the ISLR is typically used as a measured of the quality of the point-target response for SARs, it does not constitute a very representative measure of the quality of the interferometric measurement for the particular case of oceanography. While an unweighted sinc point-target response is typically unacceptable for SARs due to the high level of its first side-lobes, which can introduce artifacts in the presence of high-intensity scatterers near the desired measurement cell, such situations rarely occur over the oceans. Furthermore, and given the high intrinsic resolution of the system compared to the required final averaged resolution, there is virtually no height difference between the main-lobe measurement and that of the near side-lobes. This topic will be further explored in section 6.6.

6.4 Sinc Interpolation

With a chirp bandwidth of BW=200 MHz, the 1/B slant-range resolution of the system is $^{c}/_{2BW} = 0.75m$. The worst-case (far-swath) delay over the swath between both antennas is $Bsin(\theta_0)|_{\theta_0=3.8^\circ} \approx 0.66m$. If the two SAR images were co-registered at the swath center, the differential delay would be 0.33 m. Since this is close to being half the instrument's range resolution of 0.75 m, differential range delays will cause severe decorrelation. The OBP implements an 8-point sinc interpolation.

The sinc interpolation formula is derived from the Nyquist-Shannon sampling theorem, and states that for a bandwidth limited signal, $x(t)$, sampled with a sampling rate f_s such that the bandwidth BW is less than f_s, the signal can be perfectly reconstructed from the samples as follows:

$$x(t) = \left(\sum_{n=-\infty}^{\infty} x_n \, \delta\left(t - {}^{n}/_{f_s}\right) \right) * \operatorname{sinc}(BW \cdot t) = \sum_{n=-\infty}^{\infty} x_n \operatorname{sinc}(\beta(f_s t - n))$$

where $\beta = {BW}/{f_s}$ is the inverse of the oversampling ratio.

A real N-point sinc interpolator truncates this infinite series. In order to reduce the spectral sidelobes caused by this truncation, we propose an improved sinc interpolator by assuming a "mirrored-symmetric" interpolating signal rather than simply periodic (Figure 26). This method has no impact on the FPGA implementation: the only difference is in the interpolation kernel, which is implemented as a look-up table in hardware.

Assuming $x(t)$ is symmetric about the start position –L and periodic with 2N.

$$x(t) = \sum_{n=-\infty}^{\infty} x_n \frac{\sin\pi(t-n)}{\pi(t-n)} = \frac{\sin\pi t}{\pi} \sum_{n=-\infty}^{\infty} x_n \frac{(-1)^n}{t-n} = \sum_{j=-\infty}^{\infty} \sum_{n=-L}^{M-1} x_{n+jN} \frac{\sin\pi(t-n-jN)}{\pi(t-n-jN)}$$

$$= \sum_{j=-\infty}^{\infty} \left\{ \sum_{n=-L}^{M-1} x_{n+j2N} \frac{\sin\pi(t-n-j2N)}{\pi(t-n-j2N)} + \sum_{n=-L}^{M-1} x_{n+(j2+1)N} \frac{\sin\pi(t-n-(j2+1)N)}{\pi(t-n-(j2+1)N)} \right\}$$

$$= \sum_{j=-\infty}^{\infty} \left\{ \sum_{n=-L}^{M-1} x_n \frac{\sin\pi(t-n-j2N)}{\pi(t-n-j2N)} + \sum_{n=-L}^{M-1} x_{N-1-n} \frac{\sin\pi(t-n-(j2+1)N)}{\pi(t-n-(j2+1)N)} \right\}$$

$$= \sum_{n=-L}^{M-1} x_n \left\{ \sum_{j=-\infty}^{\infty} \left[\frac{\sin\pi(t-n-j2N)}{\pi(t-n-j2N)} + \frac{\sin\pi(t-(N-1-n)-(j2+1)N)}{\pi(t-(N-1-n)-(j2+1)N)} \right] \right\}$$

$$= \sum_{n=-L}^{M-1} x_n w_{t-n}, \ \textit{with}\ w_{t-n} = \sum_{j=-\infty}^{\infty} \left[\frac{\sin\pi(t-n-j2N)}{\pi(t-n-j2N)} + \frac{\sin\pi(t-(N-1-n)-(j2+1)N)}{\pi(t-(N-1-n)-(j2+1)N)} \right]$$

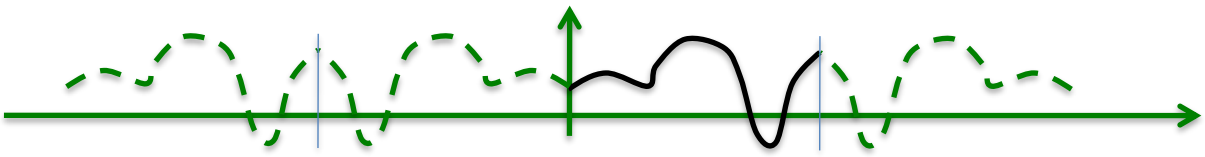

Figure 26. Perfect sinc interpolator concept

Since this new method makes assumptions about the signal that are not generally true, it is important to verify that there are no distortions in the amplitude and phase response. As shown in Figure 27 and Figure 28, for KaRIn, with 200 MHz bandwidth and 300 MHz sampling frequency, the new interpolator is better. However, in general, when the bandwidth-to-sampling frequency ratio exceeds 80%, the new interpolator would degrade the high frequency response.

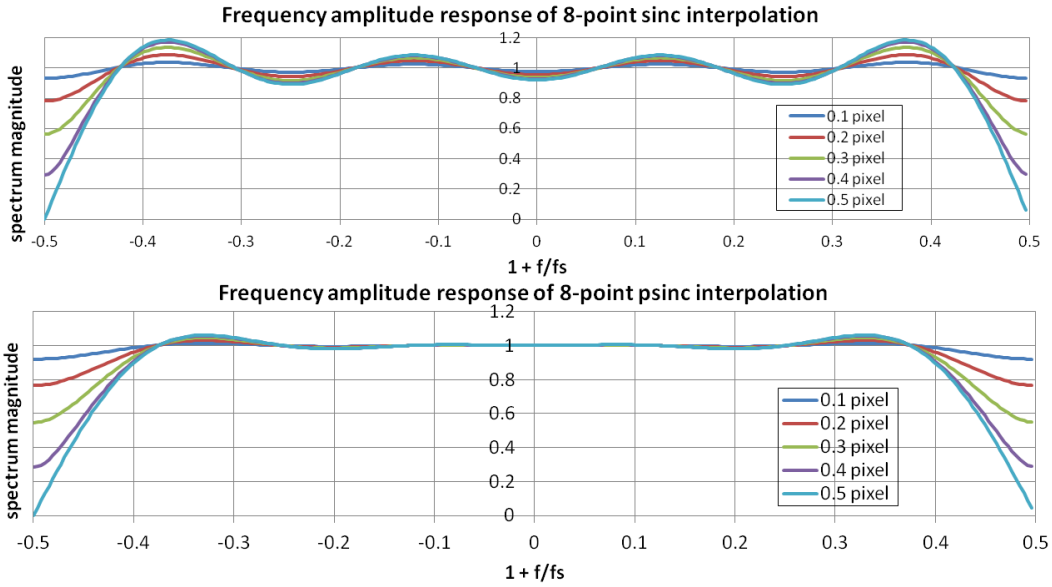

Figure 27. Comparison of the amplitude response for the 8-point perfect sinc interpolator against a regular sinc interpolator.

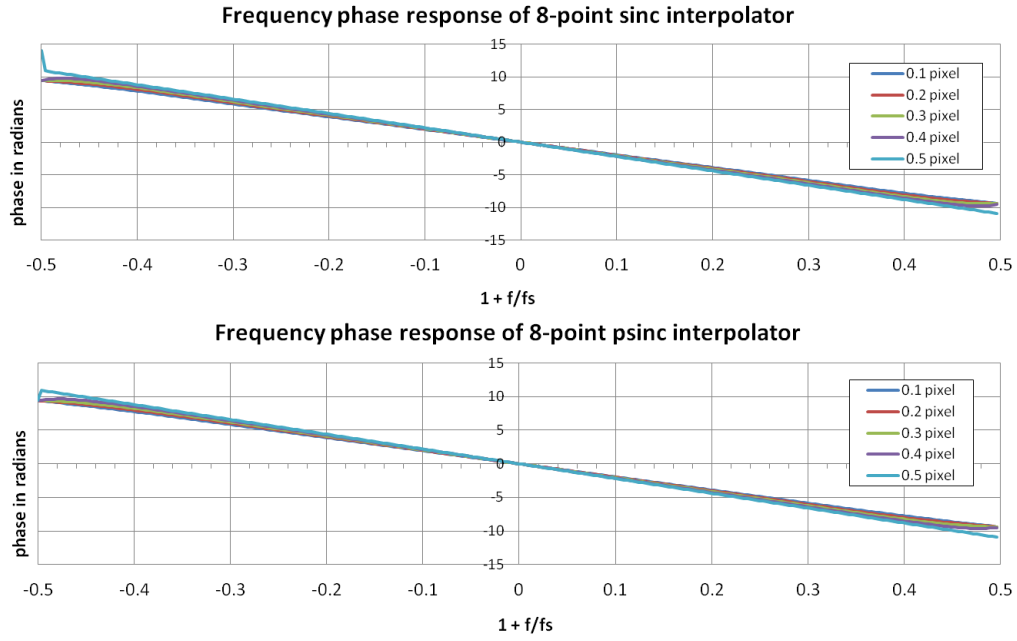

Figure 28. Comparison of the phase response for the 8-point perfect sinc interpolator against a regular sinc interpolator.

We evaluated the performance starting with a simulated range line sampled at Nyquist, and then interpolated using the improved and standard method. Figure 29 shows that the perfect sinc interpolator offers superior performance.

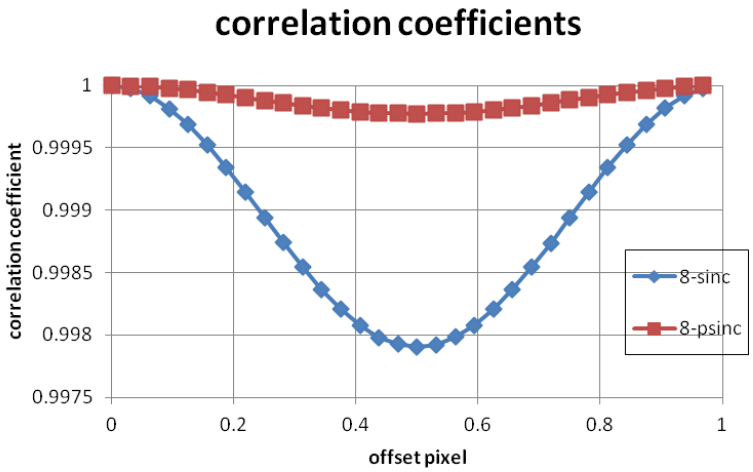

Figure 29. Comparison of the correlation coefficient for the 8-point perfect sinc interpolator against a regular sinc interpolator.

6.5 Squinted unfocused azimuth SAR processing

The azimuth compression is performed following what we call an unfocused squinted SAR approach. The on-board processor will form a number of squinted azimuth beams, N_B, for each range bin during azimuth compression by applying different phase ramps to the N_P azimuth samples, with the objective of maintaining the number of available looks. This is illustrated in Figure 30.

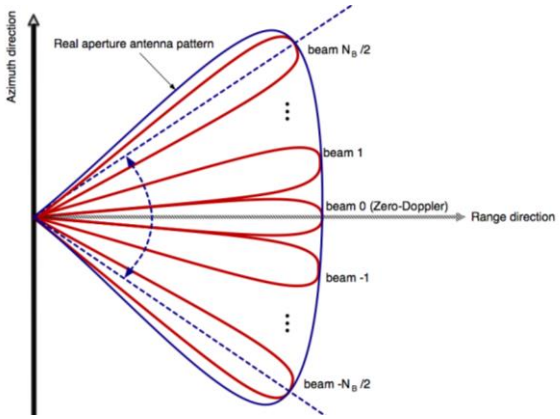

Figure 30. Illustration of the formation of N_B beams in azimuth within the 3dB real aperture beamwidth.

As explained in more detail in section 5, N_P consecutive azimuth complex values are multiplied by N_B phase ramps of the form $e^{-j2\pi m\left(\frac{J}{N_P}+\frac{f_D}{PRF}\right)}$, $m = -\frac{N_P-1}{2} \ldots \frac{N_P-1}{2}$. The indexes J are chosen by evenly dividing the processed portion of the azimuth spectrum (PBW/PRF, where PBW is the processed bandwidth) into N_B slices. A subsequent low-pass filter is implemented by performing a weighted average of the frequency shifted samples with an appropriate window.

In order to optimize hardware FPGA resources, no overlap has been implemented in the azimuth direction between consecutive sequences, so once N_P pulses have been compressed in azimuth, the next iteration will take the next N_P pulses in for compression. It is important to make sure we do not lose any looks in the process. Using a rectangular averaging window of length N_P, we obtain N_P independent looks in the PRF range. If the processing bandwidth is PBW, then we need $N_B > \frac{PBW}{PRF} N_P$. Lastly, an odd number of beams is desirable so that one of the beams is pointing at boresight.

A rectangular azimuth compression window is optimum to maintain all the looks and minimize height error (see Figure 31). A tapered window would result in lower the sidelobe to mainlobe ratio. However, in section 6.6 we will argue that, given the high correlation of the ocean scene, the impact of the sidelobe ambiguity is negligible.

The longest unfocused SAR aperture length, δa_{uSAR}, (and best attainable azimuth resolution in unfocused mode) is:

$$\delta a_{uSAR} = r\theta_{uSAR} \approx r\frac{\lambda}{2L_{uSAR}} = r\frac{\lambda}{2\sqrt{\lambda r/2}} = \sqrt{\frac{\lambda r}{2}} \approx 62\ m$$

where the range, r, is approximately the platform height (given SWOT range of look angles), θ_{uSAR} is the smallest azimuth antenna beamwidth that can be synthesized such that the difference between the minimum and maximum (two-way) path is 1/8th of the wavelength and L_{uSAR} is the corresponding synthetic aperture antenna effective length. The number of pulses in the maximum unfocused SAR length is $N_P = PRF \cdot \frac{\delta a_{uSAR}}{v_{sc}} \approx 37$, where v_{sc} is the spacecraft's velocity (roughly 7.4 km/s). This is an upper bound for the number of pulses to process.

The minimum resolution, δa_{min}, places a bound on the minimum number of beams to process, $N_B > r\frac{\theta_{bw}}{\delta a_{min}}$, with θ_{bw} the antenna beamwidth. For $\delta a_{min} = 1km$ and $\theta_{bw} = 0.1°$, we obtain $N_B \geq 2$.

High resolution is beneficial to reduce the sensitivity of the systematic phase bias correction to the antenna gain and sigma-0 characteristics (see Equation (29)). However, the correlation time for the ocean, τ_{ocean} at Ka band has been shown to be on the order of 3ms [14], which would give a bound of $N_p < \tau_{ocean} \cdot PRF = 13$ pulses. Another important consideration is that, since we are not using overlapping windows, if the ocean correlation is shorter than expected, we would be throwing away looks and the random error would increase.

Another important trade off is the selection of the processing bandwidth. Usually a larger processing bandwidth improves resolution, hence the number of looks and the random error, but at the expense of degraded azimuth ambiguities. In our case, the PRF oversamples the Doppler bandwidth ($PRF/\Delta f_{D(-3dB,1-way)} \cong 1.36$), and reducing slightly the processing bandwidth does not affect performance. Figure 31 shows the height error starts increasing below PBW/PRF ~ 0.8. As explained in section 6.6, the impact on ambiguities is small.

Due to the short integration time, wave motion effects are negligible [11].

With all the previous considerations in mind, the parameters in Table 3 have been selected.

Number of processed pulses	9
Number of beams	9
Azimuth compression window	Rectangular
PBW/PRF	0.8

Table 3. Azimuth compression algorithm parameters

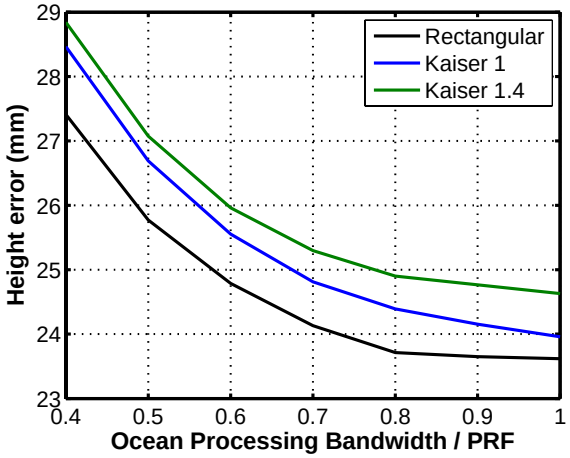

Figure 31. Height error in mm as a function of processing bandwidth relative to PRF for typical SWOT parameters and three different azimuth windows: a rectangular window and Kaiser windows with beta parameter 1 and 1.4 [17].

6.6 Interferogram formation

For *every* beam, the following products are computed:

Interferogram (complex): $u_1^{(J)} u_2^{(J)*}$

Both SAR images (real): $u_1^{(J)} u_1^{(J)*}$ and $u_2^{(J)} u_2^{(J)*}$

These, together with receive only noise measurements, allow computation on the ground of coherence, from which one can derive SWH and standard deviation of SSH.

6.7 Phase flattening

The next step in the OBP algorithm is to multiply the interferogram by a range dependent phase ramp in the time domain, which is calculated using the platform altitude and topography height over a reference sphere. The reference sphere radius is fixed and corresponds to that of the sphere tangent to the ellipsoid at 45 deg latitude along the cross track direction (see Appendix D for the residual height of the ellipsoid over the reference sphere).

6.8 Multi-look averaging

After azimuth compression (beam formation), the on-board processor performs both along-track and cross-track averaging to significantly reduce the output data rate. Separate widows are used in range

and azimuth. The range window is computed on the fly by the OBP, whereas the azimuth window is stored in an uploadable static table.

The transfer function of a rectangular window has very high side lobes, so it does not optimally filter high frequency noise and spurs, introduced by the scene itself, like ocean waves, by the instrument electronics or by the mechanical structure. The OBP implements averaging with overlapping windows, whose length is selected such that the auto-correlation at +/- half the pixel resolution is 0.5 (see Figure 32 and Figure 33), which is approximately equivalent to conserving the number of looks. In azimuth, a Blackman-Harris window has been selected for its superior high frequency rejection (see Figure 33), whereas in range a Parzen window will be used for its simplicity to compute in hardware.

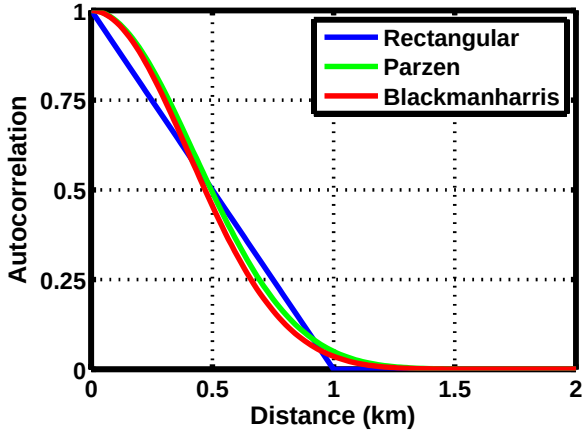

Figure 32. Averaging window autocorrelation at 1km resolution for rectangular (blue), Blackman-Harris (red) and Parzen (green) averaging windows.

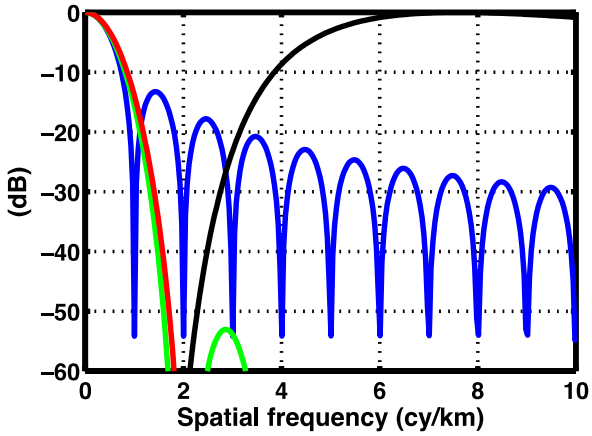

Figure 33. Transfer function for rectangular (blue), Blackman-Harris (red) and Parzen (green) averaging windows. The black curve is the Pierson-Moskowitz wave spectrum.

The number of looks in azimuth after averaging all beams is approximately given by:

$$N_{looks-az} \cong \frac{\Delta y \cdot PRF}{v_{gnd}}$$

where Δy is the azimuth multilook resolution and v_{gnd} is the ground velocity. Note that the spatial resolution is slightly worse than Δy due to the finite resolution of the azimuth point target response. However, the impact of this is negligible since the science requirement resolution is 10km and the ocean scene is highly correlated.

Azimuth ML resolution, Δy	~ 500m
Azimuth window	Blackman-Harris
Azimuth window length	72 azimuth compressed lines ~ 1km
Azimuth posting	18 azimuth compressed lines ~ 250m
Range ML resolution, Δx	500m
Range window	Parzen-like
Range window length, L_x	0.98 km
Range posting	250m

Table 4. Multi-look averaging algorithm parameters

The ground range for a given range index changes along the orbit due to platform altitude variations. The OBP uses the look angle calculation to compute ground range, and determine the ground range interval for averaging based on the window length needed to achieve the cross-track resolution, Δx, for a given averaging window type. A window similar to the Parzen window [12] is used as follows:

$$w_x(x) = \begin{cases} 1 - 6\left(\frac{2|x - x_0|}{L_x}\right)^2 + 6\left(\frac{2|x - x_0|}{L_x}\right)^3 & |x - x_0| \le \frac{L_x}{4} \\ 2\left(1 - \frac{2|x - x_0|}{L_x}\right)^3 & \frac{L_x}{2} \ge |x - x_0| > \frac{L_x}{4} \end{cases}$$

where x_0 is the ground track at which the average height is computed.

The fact that the ground range is not uniformly sampled introduces a small bias on the data, as will be discussed in section 7.2.

The number of azimuth lines used for along track averaging is fixed, which means that the azimuth posting and resolution varies by at most +/- 5% due to orbital variations in platform altitude, i.e. ground velocity, and PRF. Table 4 summarizes the parameters used for multi-look averaging.

As shown in Appendix A, the effective point target response after multi-look averaging can be obtained as a weighted average of the point target response, and the degradation due to the azimuth and range sidelobes can be computed using the average point target response.

Figure 34 shows the ideal azimuth response corresponding to the azimuth averaging window (blue), the azimuth point target response after resampling and averaging the N_B beams (red), and the equivalent point target response after averaging to 1km (black). The high side lobes resulting from using unweighted azimuth compression (in Figure 10) are smeared out after averaging to 1km. The effective resolution is about 12% higher than the resolution of the azimuth averaging window. Since this response is symmetric, only a topographic acceleration (or even orders in general) will cause an ambiguity error. However, deviations from the nominal antenna pattern and, most importantly, errors

in the Doppler centroid estimation, will break this symmetry. Figure 35-Figure 37 illustrate the height error due to ambiguity for velocity α=10cm/km and acceleration β=1cm/km^2. As discussed in section 7, the RMS values are in the order of 2cm/km and 0.2cm/km^2, so with an error in the Doppler estimation less than 10%, the error due to the ambiguity is less than 1mm for 80% processing bandwidth. (Note that to generate Figure 36 and Figure 37 the antenna pattern without dispersion was used to speed up computations).

A similar analysis applies to computing the impact of the range sidelobes. In the previous analysis, it was assumed that the antenna gain and sigma-0 where constant over the range resolution cell, but this assumption is no longer valid when computing the impact from sidelobes away from the mainlobe. Following a similar approach to that in Appendix A, the average point target response at each cross track can be shown to be:

$$\overline{\chi_x}(x) \cong \sum_{x_n} w_n \frac{G_{12}(x)\chi_x(x_n - x)}{\int G_{12}(x)\chi_x(x_n - x)dx}$$

where G_{12} here represents the product of both antennas gains and sigma-0.
Figure 38 illustrates the range point target response after averaging at 10km cross track. The average range point target response closely follows the ideal range averaging window as expected, but it extends beyond that. The error associated with the spread in the average point target response is shown in Figure 39 for velocity α=10cm/km and acceleration β=1cm/km^2. For RMS values 2cm/km and 0.2cm/km^2 the swath averaged errors are ~0.1mm and <<0.1mm respectively.

Since the azimuth and range point target response extend over a large area, they could go over land or small islands, in which case the previous analysis does not apply. Let us assume a simplified model in which the signal for each channel is a combination of the intended signal, v_{si}, and an uncorrelated spurious signal, v_{Ii}.

$$v_1 = v_{s1}e^{-j2kr_1} + v_{I1}e^{-j2kr_{I1}}$$

$$v_2 = v_{s2}e^{-j2kr_2} + v_{I2}e^{-j2kr_{I2}}$$

After processing, the interferogram is formed as follows,

$$\langle v_1 v_2^* \rangle = \langle v_{s1}v_{s2}^* e^{j\Phi} \rangle + \langle v_{I1}v_{I2}^* e^{j\Phi_I} \rangle =$$

$$= \langle v_{s1}v_{s2}^* e^{j\Phi} \rangle \left(1 + \frac{\langle v_{I1}v_{I2}^* e^{j\Phi_I} \rangle}{\langle v_{s1}v_{s2}^* e^{j\Phi} \rangle}\right) = \langle v_{s1}v_{s2}^* e^{j\Phi} \rangle \left(1 + \frac{P_I \gamma_{0I}}{P_s \gamma_{0s}}\right)$$

Note that γ_{0I} and γ_{0s} correspond to the angular and geometric correlations, but do not include the decorrelation due to thermal noise. As a worse case, we will assume that the ambiguity and the intended signal have similar correlation. The worst-case phase error is given by:

$$\partial\Phi_{max} \approx \frac{P_I}{P_s}$$

and the RMS error is

$$\partial\Phi_{RMS} \approx \frac{1}{\sqrt{2}}\frac{P_I}{P_s}$$

The swath integrated height error is:

$$\partial h \approx \frac{\sqrt{\langle x^2 \rangle}}{kB}\partial\Phi$$

Using $\sqrt{\langle x^2 \rangle}$ ≈38km, for a swath integrated RMS height error less than 0.1mm, the signal to ambiguity ratio has to be better than ~45dB.

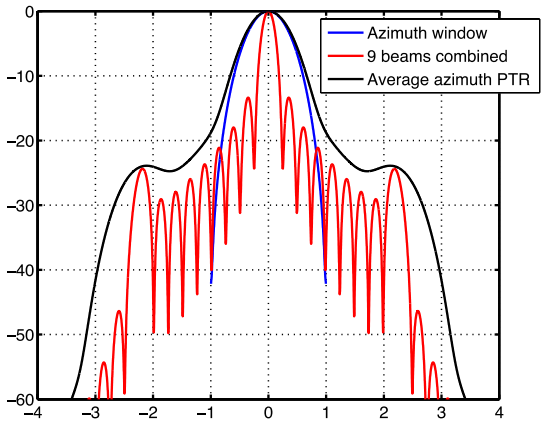

Figure 34. Azimuth point target response: azimuth averaging window (blue), after resampling and averaging the N_B beams (red) and averaged to 1km (black).

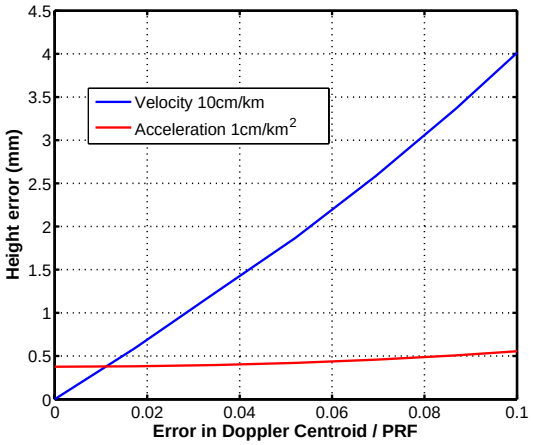

Figure 35. Azimuth ambiguity height error for 10cm/km velocity and 1cm/km^2 acceleration for PBW=0.8 and rectangular azimuth compression window.

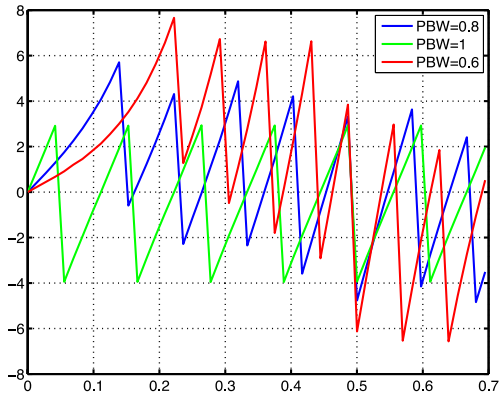

Figure 36. Azimuth ambiguity height error for 10cm/km and various processing bandwidths.

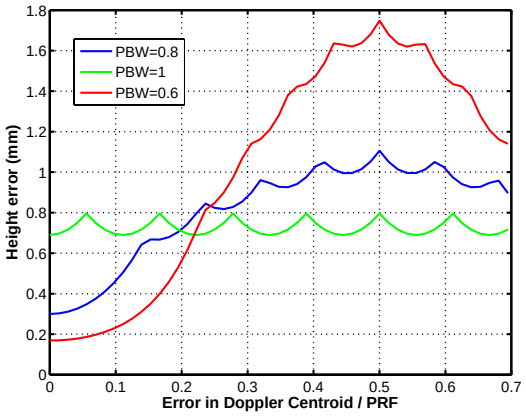

Figure 37. Azimuth ambiguity height error for 1cm/km^2 acceleration and various processing bandwidths.

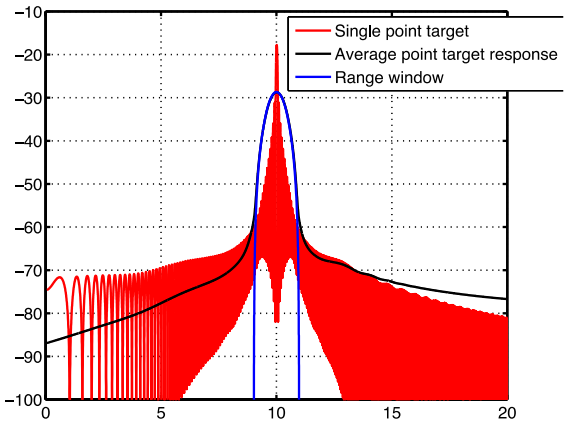

Figure 38. Range point target response at 10km: range averaging window (blue), for a single point target at 10km (red) and averaged to 1km (black).

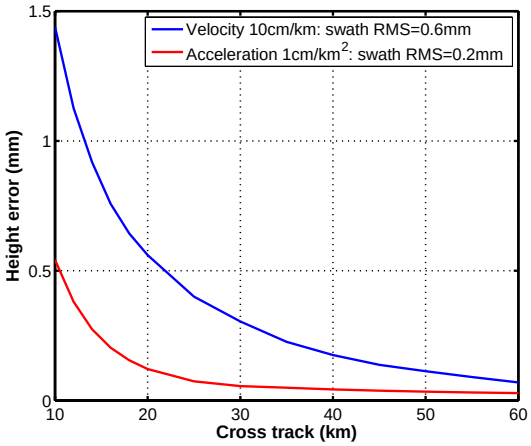

Figure 39. Height error due to range sidelobes for 10cm/km topographic velocity and 1cm/km^2 topographic acceleration as a function of cross track.

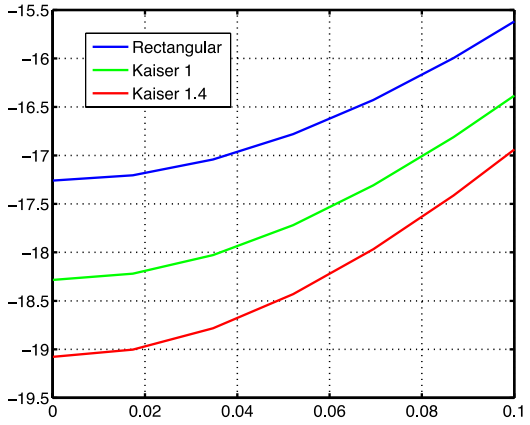

Figure 40. Azimuth Ambiguity Signal Ratio (AASR) as a function of the error in Doppler centroid estimation

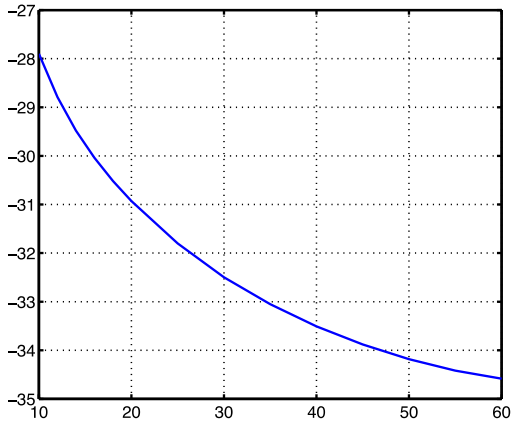

Figure 41. Integrated Sidelobe Ratio as a function of cross track

Assuming a 15dB land/water contrast, this is met for the range sidelobes for most of the swath (Figure 41). For the azimuth sidelobes, we will assume that the ocean pixel is at the edge of land (ambiguity only coming from one side of the azimuth point target response). For unweighted azimuth compression and an error in Doppler of 10%, the AASR is -15.5dB (see Figure 40), and the swath averaged RMS height error is 3.2mm.

Note that this error is not included in the error budget, since it only applies to coastal areas, and is given here for reference purposes only.

7 Description of Dynamic Algorithm

The Earth topography has a strong influence on SWOT's viewing geometry, as the distance from the platform to the surface at nadir varies with the spacecraft (S/C) position. This section will describe how the OBP adjusts for this dynamic variation along the orbit and the errors associated with it.

For each N_P pulses, flight software computes its best estimate of the platform altitude, based on DORIS information, and the topography height, and passes that information to the OBP to be used on computations of look angle, ground range and cross track averaging window. The maximum height error within the N_P pulses happens when the platform altitude changes at the fastest rate, around 45 deg latitude, at about 4m/km. The height error within the N_P pulses is then approximately <5cm, which is negligible.

The SWOT S/C uses geodetic pointing based on the WGS84 (World Geodetic System 1984) ellipsoid. The platform distance to the ellipsoid exhibits changes on the order of 25 km as shown in Figure 42. However, the actual shape of the oceans is driven by the Earth geopotential. The best "quasi-static" reference surface of the ocean is the tide-free Mean Sea Surface (MSS), which is a measure of the average height of the ocean's surface height, and exhibits variations from the WGS84 ellipsoid ranging from -105 m to 90 m. The MSS is the reference surface implemented in the OBP (see [13]).

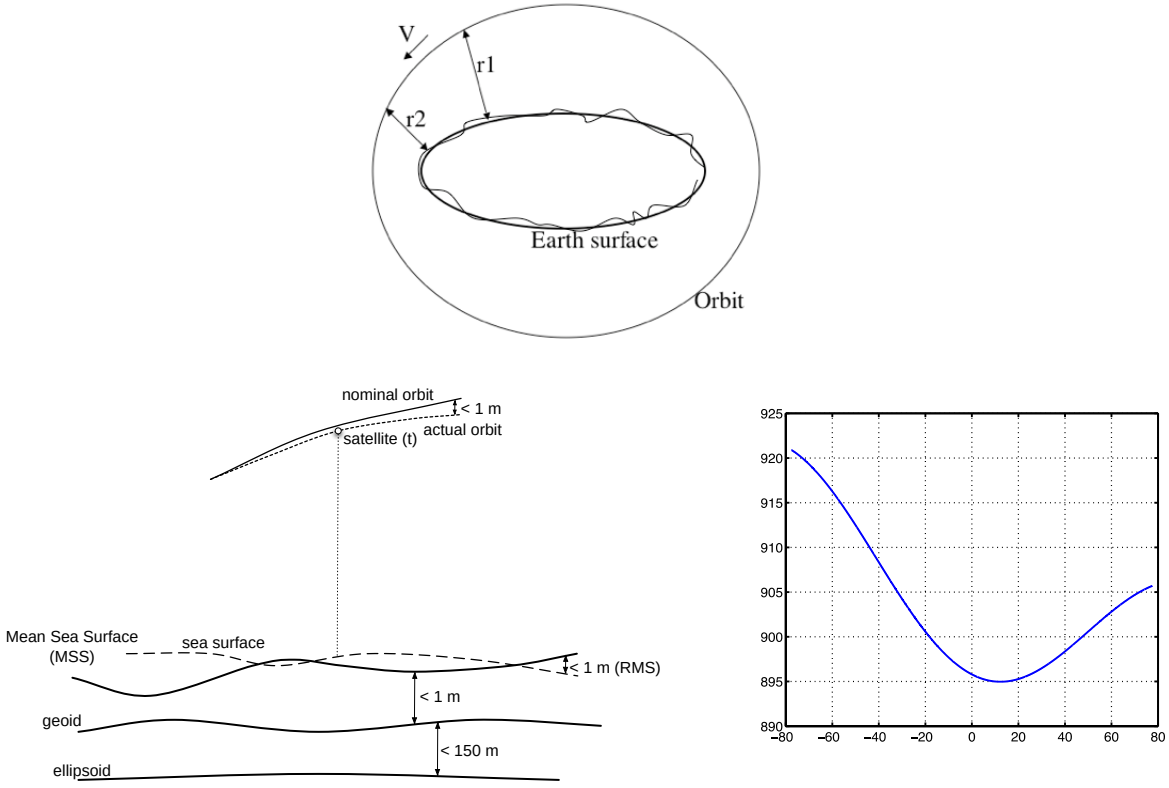

Figure 42. While the orbit is approximately circular, topography variations cause the distance between the platform and the Earth's surface to change rapidly, as shown on the left plot (not to scale). The variation of the platform altitude as a function of latitude shown on the right plot for one of the passes only considers the variations associated to the Earth's ellipsoid WGS84.

We implement a cubic spline fit approximation of the along-track MSS at the near range. This ensures that the MSS fit and the first and second derivatives are continuous. This is necessary since the along track averaging is done over overlapping windows, and there could be a discontinuity in the phase if the interpolating polynomials were not continuous. The time interval between polynomials will be adapted to MSS variations to follow the MSS with minimum error, as further explained in Appendix C.

The DORIS instrument on board provides predictions of the platform altitude, latitude and longitude every 10sec. The latitude/longitude predictions are used to navigate the MSS table and select the correct polynomial and interpolation time based on the platform predicted position.

Errors in the platform height and the MSS height result in errors in look angle, which lead to the following performance impacts on SWOT:

(1) Random error, through decorrelation.
(2) Systematic height error.
(3) Geolocation error.

Note that some of the systematic height errors, especially those due to known fields such as the reference surface, could be corrected on the ground. For this analysis, we do not assume any such corrections.

There are several sources of height uncertainty, which are analyzed in Appendix C and Appendix D and summarized in Table 5.

- **Platform altitude uncertainty**: DORIS instrument on board provides predictions of the platform altitude with an error less than 1m.
- **Pointing error:** the 3-sigma pitch error is 0.2deg, which translates into a +/3 km error in along track position. For 2cm/km (RMS) topographic acceleration (see below), the height RMS error is < 2cm.
- **Mean Sea Surface (MSS) fitting error:** The height error at 10km distance from nadir (which is the worst case for height error) is less than 0.2 meters (0.06m RMS).
- **Sea Level Anomaly (SLA).** The (tide-free) height variability above the MSL is bounded but unknown (and what SWOT is trying to measure). The study outlined in Appendix D indicates that it is at most 2 meters (0.7m RMS).
- **Tides:** The effect of tides is to introduce a (unknown) height error. We have assessed the four principal tidal constituents (M2, K1, S2, O1) and the height uncertainty is included in Table 5.
- **Reference sphere error:** The reference sphere is not an exact representation of the ellipsoid in cross track. As shown in Appendix C, this error is less than 1.5cm at 10km.

The Earth is not perfectly approximated by the MSS fitting polynomial. The residual height can be approximated to better than sub-millimetric accuracy during the averaging interval as

$$h(x) \approx h_0 + \alpha x + \frac{1}{2}\beta x^2 \tag{32}$$

where α is the topographic velocity and β the topographic acceleration and x is either cross-track or along-track distance. These topographic velocities and accelerations components are due to the residual MSS after the polynomial fit, platform height errors and the ocean topography variability. These are explained in Appendix C and Appendix D and summarized in Table 6.

Height error source	RMS	Max
Platform altitude error	1m	<1m
Pointing error	0.02m	0.3m
MSL fitting error (10km cross-track)	0.06m	0.2m
Sea Level Anomaly	0.7m	2m
Tides	O1 < 0.20 m K1 < 0.31 m M2 < 0.44 m S2 < 0.15 m	O1 < 0.54 m K1 < 0.90 m M2 < 2.25 m S2 < 0.84 m
Reference sphere deviation from ellipsoid (10km cross-track)	<0.01m	<0.02m
TOTAL (on orbit)	**1.4m RSS <2.9m SUM**	**8.1m SUM**

Table 5. Dynamic height error allocation

Table 6. Ocean topographic velocity and acceleration.

Height error source	Velocity (cm/km)	Acceleration (cm/km^2)
Platform altitude error	0.2 (RMS)	0.1 (RMS)
Along-track MSS polynomial fit	0.9 (RMS)	0.1 (RMS)
Cross-track MSS	1.8 (RMS)	0.05 (RMS)
Sea variability	0.14 (RMS)	0.007 (RMS)
Ellipsoidal Earth (cross-track)	~ 0	<0.05
TOTAL	**1.9 (RMS) <2.2 (RMS SUM)**	**0.15 RMS <0.21 (RMS SUM)**

7.1 Random error

A miscalculation of the look angle will lead to errors in co-registration and flattening that are given by:

$$\partial\Delta \cong \frac{B}{c}(\sin\theta_{OBP} - \sin\theta_0)$$

$$\partial\Omega \cong kB(\sin\theta_{OBP} - \sin\theta_0)$$

where θ_{OBP} is the look angle calculated by the OBP, and θ_0 is the real look angle. It is easy to show through basic trigonometric approximations that:

$$\partial\Delta \approx \frac{B}{c}\frac{\partial H}{\rho}$$

$$\partial\Omega \approx kB\frac{\partial H}{\rho} \tag{33}$$

where ∂H is the platform height error due to any of the sources listed below (the effect of a topography error is approximately the same as of a platform height error, and for simplicity we will refer to these conjunctly as platform height error). These equations hold true for the range of ∂H errors that we are considering here.

It can be shown that the geometric coherence when there is a co-registration error is given by:

$$\gamma_g = \frac{\int W_1(\omega + w)W_2^*(\omega)e^{-j\omega\,\partial\Delta}d\omega}{\sqrt{\int|W_1(\omega + w)|^2 d\omega \int|W_2(\omega)|^2 d\omega}}$$

If we neglect the spectral frequency shift and assume ideal square range compressed pulse and spectral filter, the decorrelation is is given by:

$$\gamma_g \approx \mathrm{sinc}(BW \cdot \partial\Delta)$$

Figure 43 shows the increase in height error as a function of the degradation in correlation factor (assumed the same across the swath) for typical SWOT parameters. A correlation factor of 0.999 makes the error negligible. This would correspond to $\partial\Delta = 120\mathrm{ps}$, and, using (33), $\partial H = 36m$ in the near range (worst case). This is well above the expected platform altitude error, and the dynamic error is dominated by the impact on $\partial\Omega$, as explained below.

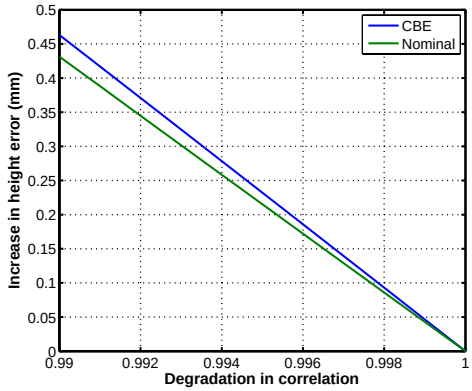

Figure 43. Increase in height error as a function of the degradation in correlation factor (assumed constant across the swath) for baseline SWOT parameters

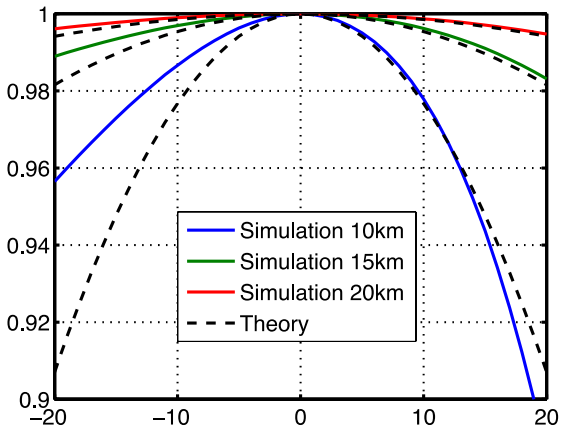

Figure 44. Coherence relative to no platform error at various points in cross-track as a function of platform height error. Dashed black curve is the approximate theoretical expression.

A flattening error will create a ramp across the swath, which will increase the phase variance, therefore resulting in increased decorrelation. From Equation (33), one can calculate the mean correlation in a cross-track averaging interval $\Delta\rho$ centered at a cross-track distance ρ_0. The dynamic correlation due to platform height errors is then given by:

$$\gamma_{DYN} \approx 1 - \frac{1}{24}\left(kB\partial H \frac{\Delta\rho}{\rho_0^2}\right)^2 \tag{34}$$

For a decorrelation less than 0.999 at the near range (10km), the platform height error has to be less than 2m. The error decreases rapidly as one moves to the far range.

Figure 44 shows the coherence relative to no platform height error as a function of platform height error at various cross tracks for both simulation and the theoretical expression in (34). This figure does not purposely include the fact that the ground averaging windows is not computed correctly, since the correct ground range will be known on the ground. The error on the ground averaging window introduces a systematic error that will be explored in section 7.2. The asymmetry in the correlation is due to the impact of the spectral shift and filtering, which was not incuded in our simple derivation of (34). For platform height error <3m, the degradation of the swath average error is <0.01mm, and the worst case error at 10km is <0.1mm.

7.2 Systematic error

The on-board processor performs both along-track and cross-track averaging of the measured interferometric phase to significantly reduce the output data rate. The dominant systematic error is due to the fact that the factor κ_z in equation (27) is a function of cross track and that the range averaging window is not sampled uniformly in ground range, since the radar echoes are uniformly sampled in range. The error, as illustrated in Figure 45, depends on the uncertainty in the platform height, and is exceedingly small.

7.3 Geolocation errors

For an error δH is the platform height, there is an error $\delta\rho \approx \frac{\delta H}{\sin(\theta_0)}$ in the cross track position. For δH=1m, $\delta\rho$ ranges from 80m in the near range (10km cross track) to 13m in the far range (60km cross track). This geolocation error will result in pixels that are shifted and with different resolution than the nominal values, but the impact of this can be corrected on the ground.

Given the residual velocity 2cm/km and acceleration 0.2cm/km^2, and for an averaging pixel of 1km, the RMS shift within the pixel is < 1cm, which results in averaging pixel shifts of <1m in the near range, which is a negligible fraction of the pixel resolution.

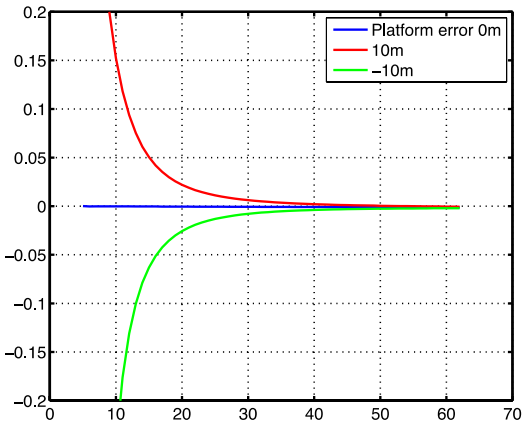

Figure 45. Height error as a function of cross track due to nonlinearity of η(x) and non-uniformly spaced range averaging window for α=10cm/km and various platform altitude errors.

8 Error Budget

As explained in section 5, the error budget for the OBP can be split into systematic errors and random errors. Both these errors are either bounded by control requirements to the instrument or to the OBP, or, if geophysical, then bounded by the 1σ case, to ensure that the overall error performance is bounded. Ground processing errors are not part of the OBP.

We have used the following assumptions, which are consistent with the analysis presented in this document:

1 3 m platform/MSS/sea topography error
2 2 cm/km topographic velocity
3 0.2 cm/km^2 topographic acceleration
4 Doppler centroid estimation better than 10% (including misalignment of antenna deployment)
5 1-sigma attitude errors

8.1 Systematic bias error

Systematic bias errors are phase/height biases, not necessarily constant across the swath, that do not decrease by averaging. The OBP systematic error is dominated by range and azimuth ambiguities and it is less than 1mm (see section 6.8).

8.2 Random error

These errors increase the variance of the phase/height estimates. The contribution of the OBP is through decorrelation and loss of effective looks. The current design of the OBP algorithm performs unweighted range and azimuth compression, and the loss of effective looks is negligible.

As further explained in section 9, the analytical model describes system performance very accurately, and will be used to assess the impact of the various contributions.

Figure 46 shows the coherence for the main contributions, and Figure 47 is the height error. Only the angular, geometric and dynamic decorrelations are part of the OBP random error budget.

8.3 Ground Processing Errors

The ground processing is in charge of beam combining, resampling and conversion from phase into height maps. This process can introduce errors.

1. Some of these errors have to do with the attainable performance when removing the systematic error biases in the presence of other error sources (e.g. baseline dilations, attitude errors, etc.)

2. Some of these errors are related to converting the phase to height, and in the final resampling and averaging.
3. Some of the processing may result in geolocation errors.

These errors lie outside the on-board processor itself and are not part of the OBP error budget.

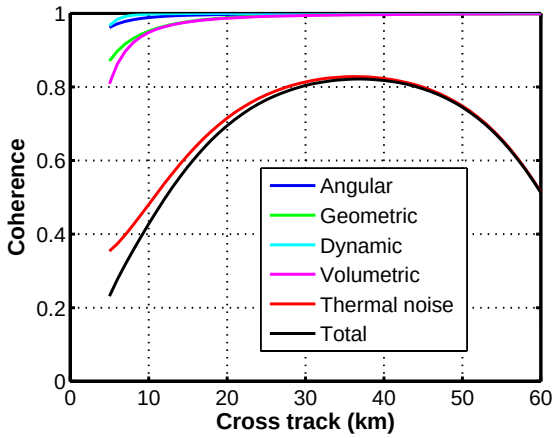

Figure 46. Coherence vs. cross track for the middle beam and SWH=2m. Only the angular, geometric and dynamic decorrelations are part of the OBP random error budget.

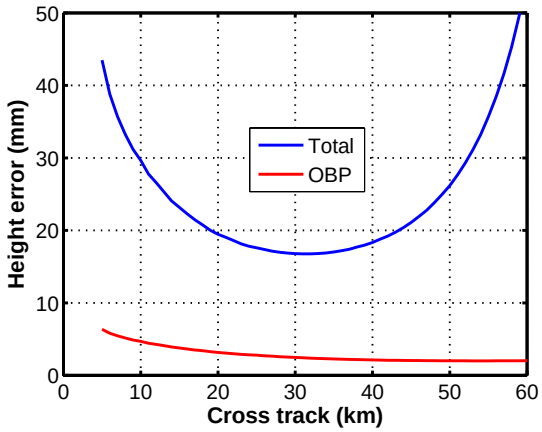

Figure 47. Height error vs. cross track. The OBP contribution is due to angular, geometric and dynamic decorrelation. The swath average error is 2.7mm for the OBP and 25.4mm total.

9 Algorithm performance simulations

The development process to validate the OBP is shown in Figure 48. A Point Target Simulator has been developed that allows simulation of raw data (radar echoes), as well as range compressed data for increased computational speed. This data is processed through a floating point model (so called golden model), a bit true model, and ultimately the hardware implementation. The output of the golden model is the complex interferogram and the power images, which are the input to the ground processing block that produces the height. Performance compliance is assessed by computing the random height error and the systematic height bias error.

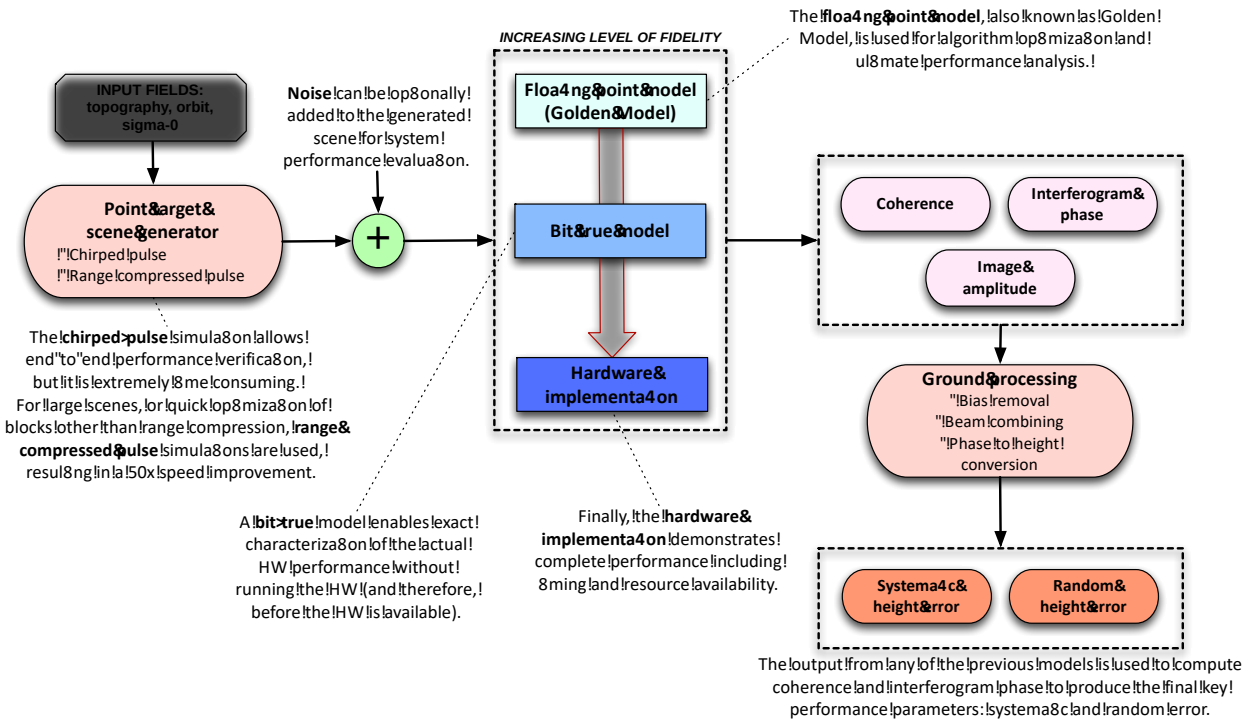

Figure 48. Development process overview

9.1 Scene #1: No topography

We simulated a scene with no topography and spherical Earth. The raw data simulation included 100 targets per resolution cell. This simulation validates the theoretical expressions for the angular, geometric and noise correlations in equations (20)-(23) both in magnitude (decorrelation) and phase (systematic bias).

Figure 49 and Figure 50 illustrate the nearly perfect match between the coherence and systematic bias obtained from raw data and that simulated by integrating the expressions in Equation (23). Both angular and geometric correlations have been included in the analysis. Figure 52 includes the effect of nominal SNR with 5dB margin. Figure 51 shows the height error as a function of cross track with and without thermal noise, after combining all beams as explained in Appendix E. It also shows the error associated with the OBP, which corresponds to the geometric and angular decorrelations.

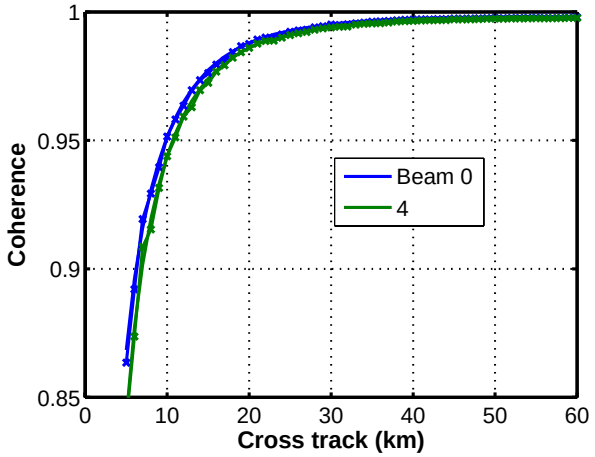

Figure 49. Coherence from raw data (crosses) and simulated (solid) by equations (20)-(23) for the center and outer beam

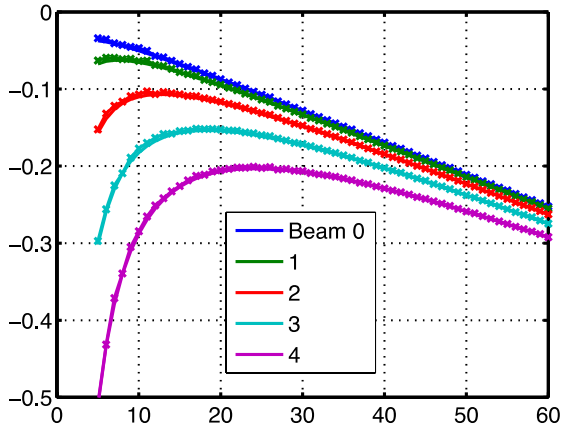

Figure 50. Systematic bias from raw data (crosses) and simulated by equation (20)-(23)

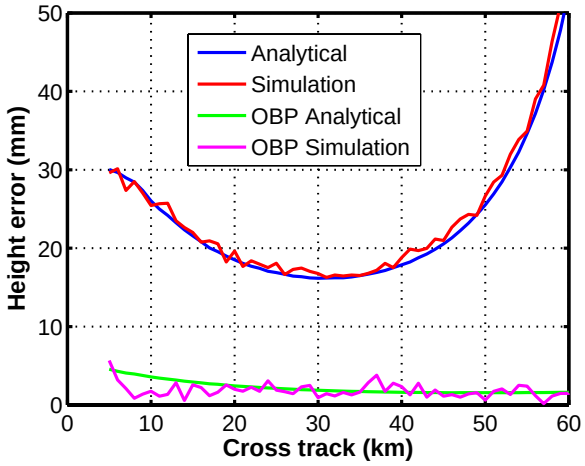

Figure 51. Height error as a function of cross track (no topography and no waves)

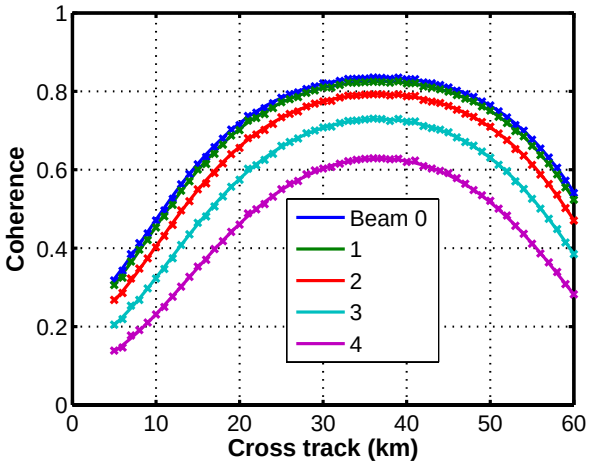

Figure 52. Coherence from raw data (crosses) and simulated by equation (23) when adding thermal noise.

9.2 Scene #2: Waves

We have simulated multiple speckle and spectral realizations for a Wavewatch-III spectrum with SWH=2.8. As can be observed in Figure 53, the main wave field is aligned close to the cross track direction and the wavelength centroid is ~290m. A detail of the ocean wave scene is included in Figure 54.

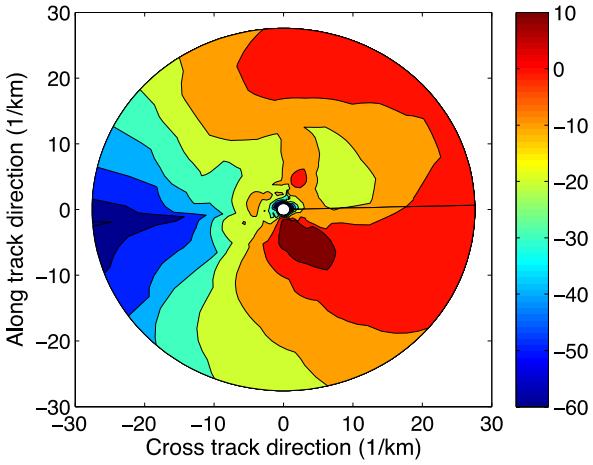

Figure 53. WaveWatch-III spectrum

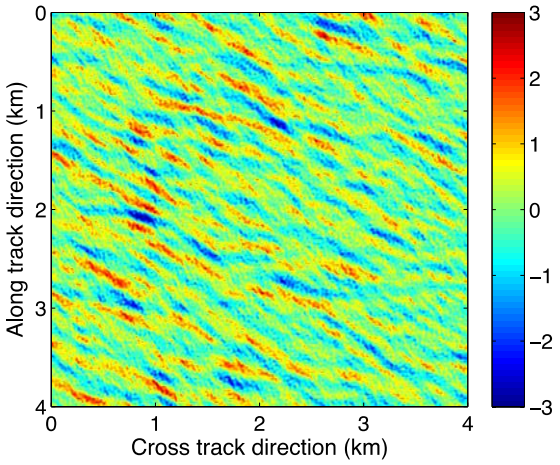

Figure 54. Detail of ocean wave scene.

Figure 56 shows the measured coherence as a function of cross track for the center beam, with and without thermal noise. The solid lines, which agree well with the average coherence, have been calculated using the volumetric formulation in section 5.4 to characterize the effect of the ocean waves. The ripple and the increased bias in the near range are due to the surf-board effect, as explained in [18].

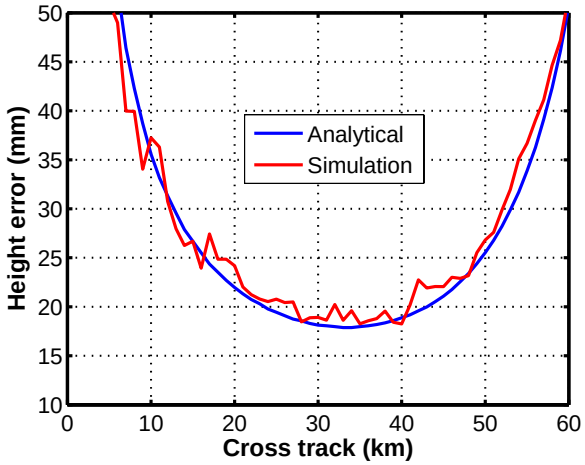

Figure 55. Height error as a function of cross track (with waves and thermal noise)

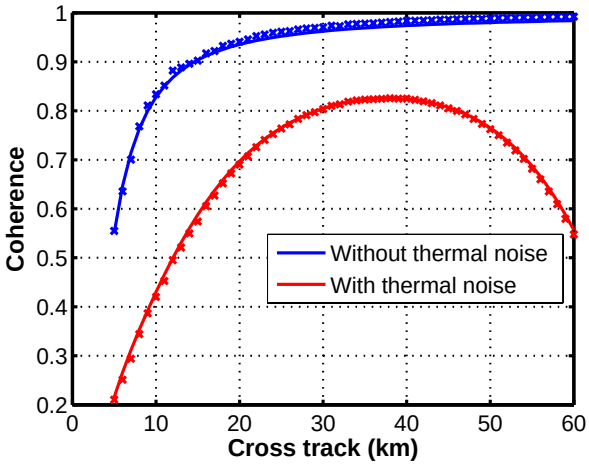

Figure 56. Measured coherence for the center beam with (red) and without (blue) thermal noise. The solid lines are the theoretical correlation using the volumetric formulation to characterize the wave effect.

Appendix A. Impact of range sidelobes and azimuth ambiguities on performance

The measured complex interferometric signal can be approximately expressed as a convolution of the range and azimuth interferometric point target responses with the interferometric phase that is due to the topography. For the ocean, and given the fact that we are flattening the interferometric phase referenced to the mean sea level, this term is small. Thus, we can approximate the measured height at a pixel (x_0, y_0) as follows:

$$h_{meas}(x_0, y_0) \approx \iint dS\, h(x,y)\chi_x(x - x_0)\chi_y(y - y_0)$$

where $h(x,y)$ is the local sea level height. In the previous expression, the cross-track point target response, $\chi_x(x)$, includes the effects of range compression and spectral filtering, whereas the along-track interferometric point target response, $\chi_y(y)$, includes the antenna azimuth ambiguities and the beam formation. They are normalized such that $\int \chi_{x,y}(u)du = 1$.

After multi-look averaging with cross-track, $w_x(x)$, and along-track $w_y(y)$, windows, the measured height is given by:

$$\overline{h_{meas}(x_0, y_0)} \approx \iint dS\, h(x,y)\overline{\chi_x}(x - x_0)\overline{\chi_y}(y - y_0)$$

where

$$\overline{\chi_{x,y}}(x_0) = \int w_{x,y}(x)\chi_{x,y}(x_0 - x)dx$$

The averaging windows are normalized such that $\int w_{x,y}(u)du = 1$.

The signal acquired through the sidelobes will be highly correlated with the topography that is being measured by the main lobe. Given that the ocean topography is very smooth, the associated error will be small. The height error associated with the presence of sidelobes/ambiguities is given by:

$$\delta h \approx \iint dS\, h(x,y)\overline{\chi_x}(x)\overline{\chi_y}(y) - \iint dS\, h(x,y)w_x(x)w_y(y)$$

Note that this error can be reduced with increased complexity of the ground processing algorithm.

Appendix B. MLE estimator for combining the beams

If the number of looks is large, from the asymptotic behavior of the MLE estimator, the height from each beam will be Gaussian distributed. If the uniform phase estimator is unbiased, as it is for a large number of looks, and assuming that the heights from each beam, h_i, are uncorrelated, the MLE for the height will be given by:

$$\hat{h} = \sum_{i=0}^{N_B} w_i h_i$$

$$w_i = \frac{1}{\sigma_{hi}^2 \sum_{j=1}^{N_B} \sigma_{hj}^{-2}}$$

The expected variance of the estimate is also well known:

$$\sigma_h^2 = \frac{1}{\sum_{j=1}^{N_B} \sigma_{hj}^{-2}}$$

Appendix C. Dynamic approximation to MSS

The OBP uses a spherical reference for phase flattening. However, the Earth is best approximated by an ellipsoid, and the deviation from the reference sphere will result in a height error, as well as a topographic velocity and acceleration. The reference sphere used by SWOT OBP has the radius of the sphere tangent to the ellipsoid at 45 deg latitude along the cross track direction. As illustrated in Figure 57, the height error is minimal at the near range (<1.5cm at 10km). The dependence along track can be very well described by a quadratic polynomial such as in (32). The acceleration is less than 0.05cm/km^2 (Figure 58) and the velocity is negligible (<0.01cm/km).

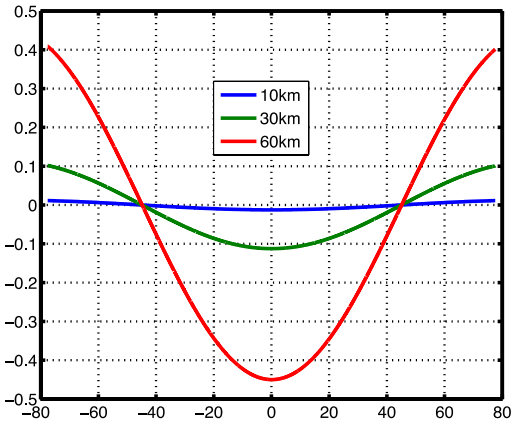

Figure 57. Ellipsoid height over reference sphere as a function of latitude for various cross-track distances from nadir.

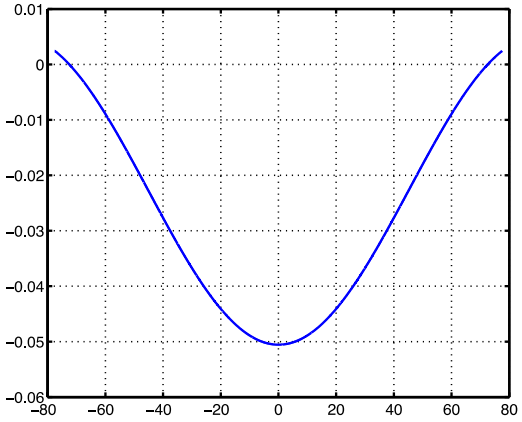

Figure 58. Acceleration of ellipsoid as a function of latitude.

SWOT will use the tide-free Mean Sea Surface (MSS) as the reference ocean surface over the ellipsoid (see [13]). The MSS will be implemented in the OBP as a cubic spline fit approximation of the along-track MSS at the near range. This will ensure that the MSS fit and the first and second derivatives are continuous. This is necessary since the along track averaging is done over overlapping windows, and there could be a discontinuity in the phase if the interpolating polynomials were not continuous. The time interval between polynomials will be adapted to MSS variations to follow the MSS with minimum error with the constraints shown in Table 7.

The reference surface is not a perfect representation of the MSS, and there remain not only errors in height, but also residual topographic velocity and acceleration components. These are illustrated in Figure 59 through Figure 63. The spacing used to compute these components is 2km, which is consistent with the resolution of the data and the spatial scale of interest.

Table 7. Dynamic algorithm parameters

Maximum update rate for polynomial	1 sec
Mean update rate for polynomial	10 sec
Maximum height error for land	1m
Maximum height error for ocean	0.2m

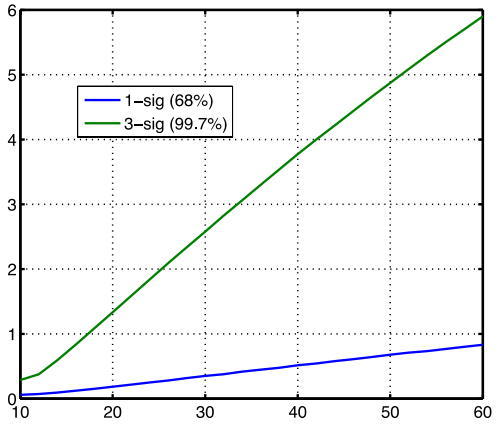

Figure 59. Residual MSS height over the ellipsoid as a function of cross-track distance.

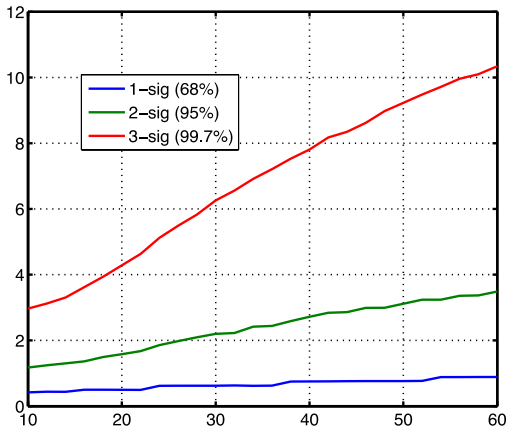

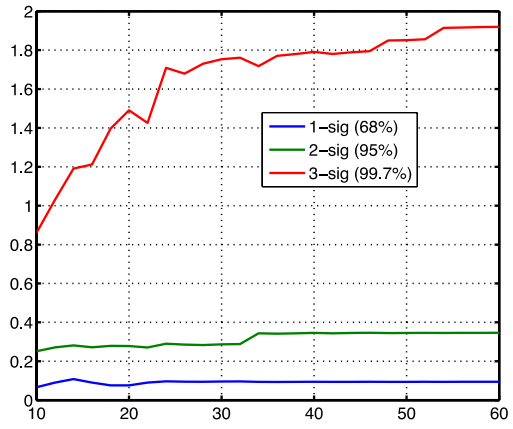

Figure 60. Residual MSS along track topographic velocity over the ellipsoid as a function of cross-track distance.

Figure 61. Residual MSS along track topographic acceleration over the ellipsoid as a function of cross-track distance.

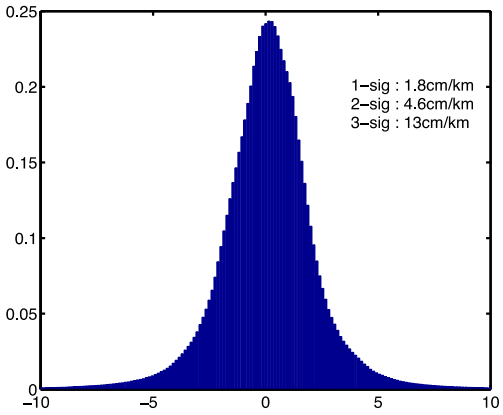

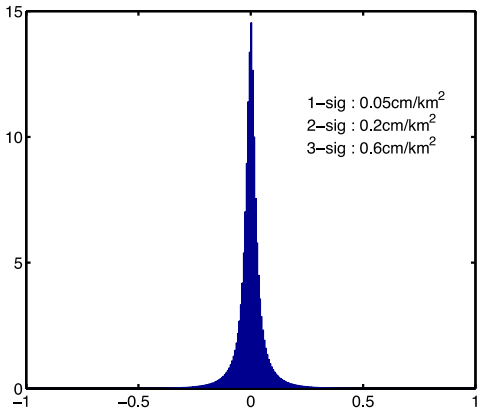

Figure 62. Histogram of MSS cross track velocity over the ellipsoid

Figure 63. Histogram of MSS cross track acceleration over the ellipsoid

Appendix D. Ocean topography variability

We have investigated the tide free ocean topography variability topography using ECCO2 (Estimating the Circulation and Climate of the Ocean, Phase II) data. ECCO2 produces accurate syntheses of all available global-scale ocean and sea-ice data at high resolution. ECCO2 data syntheses are obtained by least squares fit of a global full-depth-ocean and sea-ice configuration of the Massachusetts Institute of Technology general circulation model (MITgcm) to the available satellite and in-situ data.

Figure 64 shows the mean sea level variability obtained from processing one month of ECCO2 data. Figure 65 is a histogram of the data. The sea level anomaly is less than 2 meters, with an RMS value of 0.7m.

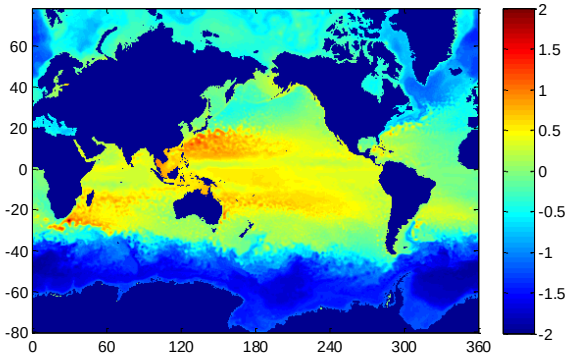

Figure 64. Mean height (m) due to sea variability from ECCO2 simulation data.

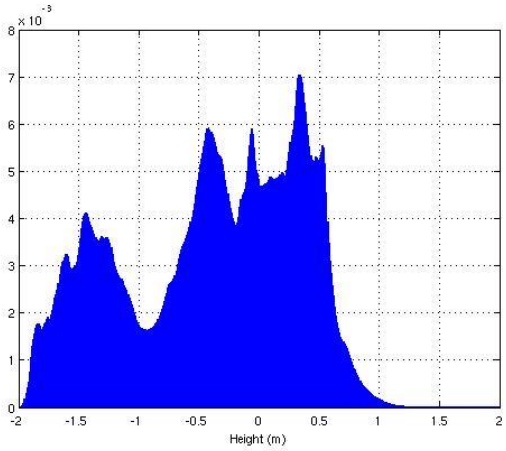

Figure 65. Histogram of height due to sea variability from ECCO2 simulation data.

The topographic velocity and acceleration from the ECCO2 data is as follows:

1. 0.14 cm/km 1-sigma sea variability velocity
2. 0.007 cm/km^2 1-sigma sea variability acceleration.

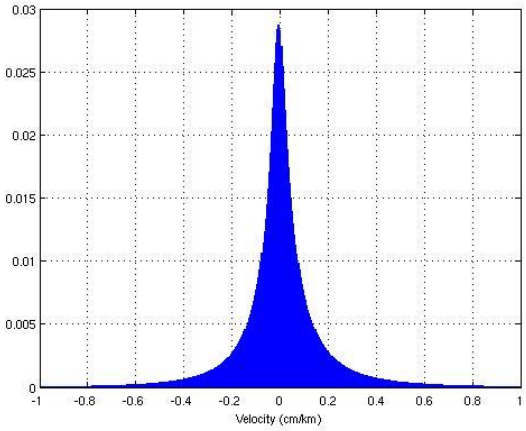

Figure 66. Histogram of velocity due to sea variability from ECCO2 simulation data.

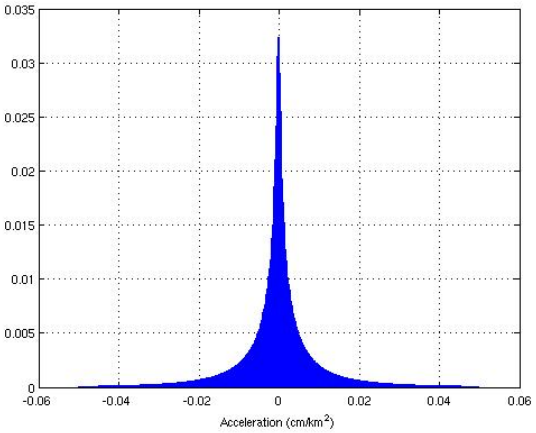

Figure 67. Histogram of acceleration due to sea variability from ECCO2 simulation data.

Appendix E. OBP pseudo-code

Golden Model Top Module

Input: rawdataL, rawdataR
Output: fD, intFNML, sarRML, sarLML

```
1   Estimate Doppler centroid for left channel
            Input: rawdataL
            Output: fDL

2   Estimate Doppler centroid for right channel
            Input: rawdataR
            Output: fDR

3   Compute mean Doppler centroid
            Input: fDL, fDR
            Output:
                  fD = (fDL + fDR)/2

4   Form SAR image for left channel
            Input: rawdataL, fD
            Output: sarL

5   Form SAR image for right channel
            Input: rawdataR, fD
            Output: sarR

6   Form interferogram and power images:
            Input: sarR, sarL
            Output:
                  intFN = sarR * conj(sarL)
                  powR = sarR * conj(sarR)
                  powL = sarL * conj(sarL)
6   Phase flattening

      Loop through all lines in blocks of NP and for every range gate:

            Compute phase ramp exp(1i*kB/2*sin(look_angle))
```

Loop through all lines:

Multiply interfeorgram by phase ramp

7 Convolve in range and azimuth with averaging windows

Input: intFN, sarR, sarL

Output: intFNML, sarRML, sarLML

Estimate Doppler centroid

Input: rawdata
Output: fD

1 Calculate pulse pair phase difference in azimuth

2 Convolve pulse pair phase difference in range and azimuth with averaging windows

3 Compute unwrapped phase

4 Compute linear fit to unwrapped phase as a function of ground range

Form SAR image

Input: rawdata, fD
Output: sar

1 Range compression

Loop through all lines:

Pad with zeros to 8192 points

Compute FFT of sar

Multiply by reference function

Compute inverse FFT

2 Look angle computation for reference surface

Loop through all lines in blocks of NP:

Compute platform height

Compute geoid height

Loop through all lines in blocks of NP and for every range gate:

Compute look angle

3 Sinc interpolation

Loop through all lines in blocks of NP and for every range gate:

Compute path delay

Loop through all lines and for every range gate:

Convolve radar echo with sinc interpolation window corresponding to path delay

4 Azimuth compression

Loop through all lines in blocks of NP and for every range gate:

Multiply by doppler phase ramp

Convolve with azimuth compression window for each beam

References

[1] P. Rosen, S. Hensley, I. Joughin, F. Li, S. Madsen, E. Rodriguez, and R. Goldstein, “Synthetic aperture radar interferometry - invited paper,” Proceedings of the IEEE, vol. 88, no. 3, pp. 333–382, 2000.

[2] J. Curlander and R. McDonough, Synthetic Aperture Radar: Systems and Signal Processing. Wiley-Interscience, 1991.

[3] R. Carande, “Estimating ocean coherence time using dual-baseline interferometric synthetic aperture radar,” IEEE Transactions on Geoscience and Remote Sensing, vol. 32, no. 4, 1994.

[4] Rodriguez, E., and J. M. Martin. "Theory and design of interferometric synthetic aperture radars." *Radar and Signal Processing, IEE Proceedings F*. Vol. 139. No. 2. IET, 1992.

[5] F. Ulaby, R. Moore, and A. Fung, Microwave remote sensing: active and passive. Vol. 2, Radar remote sensing and surface scattering and emission theory. Addison-Wesley, 1982.

[6] I. G. Cumming, F. H. Wong, “Digital processing of Synthetic Aperture Radar data”, Artech House, 2005

[7] Prati, Claudio, and F. A. B. I. O. Rocca. "Improving slant-range resolution with multiple SAR surveys." Aerospace and Electronic Systems, IEEE Transactions on 29.1 (1993): 135-143.

[8] Gatelli, Fabio, et al. "The wavenumber shift in SAR interferometry." Geoscience and Remote Sensing, IEEE Transactions on 32.4 (1994): 855-865.

[9] Papoulis, Athanasios. The Fourier integral and its applications. McGraw-Hill, 1962.

[10] V. Kudryavtsev, A. Myasoedov, B. Chapron, J. A. Johannessen, and F. Collard, “Joint sun-glitter and radar imagery of surface slicks,” Remote Sensing of Environment, vol. 120, pp. 123–132, 2012.

[11] J. Schulz-Stellenfleth and S. Lehner, “Ocean wave imaging using an airborne single pass across-track interferometric sar,” Geoscience and Remote Sensing, IEEE Transactions on, vol. 39, no. 1, pp. 38–45, 2001.

[12] http://www.mathworks.com/help/signal/ref/parzenwin.html

[13] http://www.aviso.oceanobs.com/en/news/ocean-indicators/mean-sea-level/

[14] R. D. Chapman, B. L. Gotwols, and R. E. Sterner II , “On the statistics of the phase of microwave backscatter from the ocean surface”, *J. Geophysical Research,* vol. 99, No C8. pp 16,293-16,301, Aug. 15, 1994

[15] http://polar.ncep.noaa.gov/waves

[16] Curtis Chen, “Sausage User Guide”

[17] http://www.mathworks.com/help/signal/ref/kaiser.html

[18] E. Peral, E. Rodriguez, D. Esteban-Fernandez, “Impact of Surface Waves on SWOT’s Projected Ocean Accuracy”, Remote Sensing 7(11):14509-14529 November 2015, https://www.researchgate.net/publication/283823875_Impact_of_Surface_Waves_on_SWOT's_Projected_Ocean_Accuracy